

Deformation and dislocation evolution in body-centered-cubic single- and polycrystal tantalum

Seunghyeon Lee, Hansohl Cho[†]

Department of Aerospace Engineering, Korea Advanced Institute of Science and Technology, Daejeon, 34141, Republic of Korea

Curt A. Bronkhorst[‡]

Department of Engineering Physics, University of Wisconsin, Madison, WI 53706, USA

Reeju Pokharel, Donald W. Brown, Bjørn Clausen, Sven C. Vogel, Veronica Anghel, George T. Gray III
Materials Science & Technology Division, Los Alamos National Laboratory, Los Alamos, NM 87545, USA

Jason R. Mayeur

Mechanical and Aerospace Engineering Department, University of Alabama in Huntsville, Huntsville, AL 35899, USA

E-mails: [†] hansohl@kaist.ac.kr (Hansohl Cho), [‡] cbronkhorst@wisc.edu (Curt A. Bronkhorst)

Abstract. A physically-informed continuum crystal plasticity model is presented to elucidate the deformation mechanisms and dislocation evolution in body-centered-cubic (bcc) tantalum widely used as a key structural material for mechanical and thermal extremes. We show our unified structural modeling framework informed by mesoscopic dislocation dynamics simulations is capable of capturing salient features of the large inelastic behavior of tantalum at quasi-static (10^{-3} s^{-1}) to extreme strain rates (5000 s^{-1}) and at room temperature and higher (873K) at both single- and polycrystal levels. We also present predictive capabilities of our model for microstructural evolution in the material. To this end, we investigate the effects of dislocation interactions on slip activities, instability and strain-hardening behavior at the single crystal level. Furthermore, *ex situ* measurements on crystallographic texture evolution and dislocation density growth are carried out for the polycrystal tantalum specimens at increasing strains. Numerical simulation results also support that our modeling framework is capable of capturing the main features of the polycrystal behavior over a wide range of strains, strain rates and temperatures. The theoretical, experimental and numerical results at both single- and polycrystal levels provide critical insight into the underlying physical pictures for micro- and macroscopic responses and their relations in this important class of refractory bcc materials undergoing severe inelastic deformations.

1 Introduction

Body-centered-cubic (bcc) crystalline tantalum is a refractory transition metal in the Group V. It has been widely used for key structural components often exposed to harsh physico-chemical environments due to its superb strength, ductility and corrosion and radiation resistance over a wide range of strains, strain rates and temperatures. The mechanical behavior of tantalum and its alloys has been a focal point of research to facilitate their applications in diverse mechanical, thermal and chemical extremes. Recently, these materials are also finding new avenues towards high performance metallic composites and laminates for biological, defense and energy applications (Matsuno et al. 2001; Pappu et al. 1996; Mayeur et al. 2013).

Inelasticity in bcc materials has been a long-standing interest. Inelastic deformation mechanisms in bcc materials are fundamentally different from those in face-centered-cubic (fcc) or hexagonal materials. Inelastic slip in bcc materials are governed mainly by the motion of screw dislocations in a close-packed direction of $\langle 111 \rangle$ on several different planes of $\{110\}$, $\{112\}$ or $\{123\}$. As pointed out in Lim et al. 2020, the planes where slip occurs in bcc crystals have been deemed elusive. Furthermore, inelastic slip of screw dislocations is a thermally-activated process over a wide range of strain rates and temperatures as well postulated in Stainier et al. 2002 and Nguyen et al. 2021. The high Peierls stress (or lattice friction) associated with screw dislocations and the thermally-activated formation of kink pairs give rise to strongly rate- and temperature-dependent inelastic features in bcc crystals and their alloys. Over the past several decades, the rate- and temperature-dependent inelasticity has been investigated for single crystalline tantalum (Byron 1968; Stainier et al. 2002; Lim et al. 2020; Nguyen et al. 2021) and polycrystalline tantalum (Hoge and Mukherjee 1977; Kothari and Anand 1998; Nemat-Nasser et al. 1998).

In conjunction with the experimental and theoretical studies on the rate- and temperature-dependent inelastic features due to the complex motion of screw dislocations, the breakdown of the classical Schmid law also known as non-Schmid effects has been widely reported for bcc materials since the classical work by Taylor and Elam 1926 and Taylor 1928. A non-planar core structure of the dominant screw dislocations gives rise to such abnormal plasticity features as tension-compression asymmetry and orientation-dependent critical shear stress for the onset of inelastic slip as experimentally evidenced in Byron 1968 and Sherwood et al. 1967. Moreover, the underlying physics of the non-planar core structure in $\langle 111 \rangle$ screw dislocations has been

studied via atomistic simulations (Duesbery et al. 1973; Gröger et al. 2008a; Gröger et al. 2008b; Yang et al. 2001) and ab-initio calculations (Ismail-Beigi and Arias 2000; Dezerald et al. 2016). Manifestation of non-Schmid effects has been well evidenced in experiments and atomistic simulations for tantalum materials, especially at low temperature (Dezerald et al. 2015; Sherwood et al. 1967).

Meanwhile, classical continuum models of single crystalline materials are traced back to the seminal work by Taylor 1938, Hill and Rice 1972, Asaro 1983 and Asaro and Needleman 1985. More recently, the finite deformation single crystal plasticity theory was further developed within a thermodynamically consistent framework involving both macroscopic- and microscopic force balances (Anand 2004; Gurtin 2000). Moreover, robust implicit numerical procedures for updating the constitutive models within finite deformation framework have been well established for use in nonlinear finite elements for boundary value problems of single- and polycrystal materials (Kalidindi et al. 1992; Cuitiño and Ortiz 1993; Miehe et al. 1999). Based upon these classical papers, numerous single crystal plasticity models have been proposed and have found success in elucidating the key features in the mechanical behaviors of bcc single crystals including tantalum (Nguyen et al. 2021), α -iron (Narayanan et al. 2014), niobium (Mayeur et al. 2013), tungsten (Cereceda et al. 2016) and their alloys (Chen and Gray 1996) under diverse loading scenarios over a wide range of crystallographic orientations. Moreover, as recently reviewed in Cho et al. 2018, continuum single crystal plasticity models have been extended to capture the non-Schmid behavior of tantalum and other bcc materials, especially at low temperatures, informed from atomistic simulations on the non-planar core structure of an isolated screw dislocation under diverse loading conditions.

Single crystal plasticity theories have also enabled accurate modeling of the mechanical behavior of polycrystalline materials via nonlinear finite elements. The early models of polycrystalline behaviors involving the evolution of anisotropy due to crystallographic texturing date back to the work by Asaro 1983 and Asaro and Needleman 1985 based on the classical work by Taylor 1938, in which all grains were assumed to have an equal volume and the deformation gradient within each grain was assumed to be uniform throughout the aggregate of the grains. Although these Taylor-type polycrystal models do not satisfy “compatibility” throughout the grain aggregate network, they have found success in part in modeling the nonlinear mechanical behavior and the evolution of crystallographic textures during deformation in many fcc (Asaro and Needleman 1985; Kalidindi et al. 1992; Miehe et al. 1999) and bcc materials (Kothari and

Anand 1998; Nemat-Nasser et al. 1998). Polycrystal models have been recently extended to satisfy both equilibrium and geometric compatibility, for which each of the finite elements represents one single crystalline grain (Kalidindi et al. 1992; Bronkhorst et al. 1992; Anand 2004). Furthermore, recent progress in electronic backscatter diffraction analysis of actual polycrystalline microstructures has enabled better modeling of the polycrystalline behavior with more realistic microstructures and networks of grains and grain boundaries especially for polycrystal bcc materials and laminates (Knezevic et al. 2014). However, in these papers, the details regarding constituent single crystal behavior have not been presented independently of the polycrystal behavior; i.e., the previous modeling efforts have been focused mainly on the effective responses of the polycrystals. Furthermore, as the extreme thermomechanical responses associated with shear band localization, ductile damage and spallation upon harsh loading events have recently received great attention (Bronkhorst et al. 2016; Bronkhorst et al. 2021; Kraus et al. 2021), there has been an increasing need for unified structural modeling frameworks for both tantalum single- and polycrystals at a wide range of strains, strain rates and temperatures.

This work aims at elucidating deformation mechanisms and dislocation structure evolution in bcc single- and polycrystal tantalum using a suite of theoretical modeling, numerical simulation and experimentation. We present a physically-informed finite deformation single crystal viscoplasticity model in which the underlying physics of dislocation evolution and interaction throughout the slip systems is taken into account. Then, we show the predictive capabilities of the single crystal model at strain rates ranging from 0.001 s^{-1} to 10^3 s^{-1} and at temperatures ranging from room temperature to 873K for various crystallographic orientations. The model is further validated for the inelastic features in polycrystal tantalum. To this end, we conducted an extensive set of new experiments for the polycrystal specimens including mechanical tests and *ex situ* neutron diffraction measurements on dislocation density growth and texture evolution, and compared the experimental data with the corresponding numerical simulation results. Using the unified modeling framework for both single- and polycrystal tantalum, we further develop critical insights into the inelastic deformation mechanisms at both microscopic- and macroscopic levels in this important class of refractory bcc materials.

The main body of this paper is as follows. The single crystal plasticity model is presented together with results on the single crystal behavior of tantalum from low- to high strain rates and at room temperature and higher in Section 2. Then, the single crystal model is further validated for polycrystal behaviors in both experiments and numerical simulations in Section 3,

where we directly compare experimental data for evolution of texture and dislocation density and macroscopic mechanical responses against numerical results. Finally, we briefly summarize and discuss our main conclusions on the deformation mechanisms and the dislocation evolution in single- and polycrystal tantalum at various loading conditions in Section 4. Furthermore, some numerical details used in our analysis are provided in the Appendix.

A complete list for mathematical symbols used throughout this work is given in Table 1.

Table. 1. List of symbols.

Symbol	Definition or meaning
$\mathbf{F}, \mathbf{F}^e, \mathbf{F}^p$	Total, elastic, and plastic deformation gradients
$\mathbf{R}^e, \mathbf{U}^e$	Elastic rotation, right stretch
$\mathbf{C}^e, \mathbf{E}^e$	Elastic right Cauchy-Green tensor, elastic strain tensor
$\mathbf{L}, \mathbf{L}^e, \mathbf{L}^p$	Velocity gradient, elastic and plastic distortion rates
$\dot{\gamma}_p^\alpha, \dot{\gamma}_0$	Plastic shear strain rate in the slip system α , reference slip rate
$\mathbf{m}_0^\alpha, \mathbf{n}_0^\alpha$	Slip direction and slip plane normal for slip system α
$\mathbb{S}_0^\alpha, \mathbb{S}^\alpha$	Schmid tensors in intermediate space and deformed configuration
Φ	Elastic free energy
\mathcal{C}	Fourth order elastic stiffness
$\mathcal{C}_{11}, \mathcal{C}_{12}, \mathcal{C}_{44}$	Elastic constants at current temperature
$\mathcal{C}_{11,0}, \mathcal{C}_{12,0}, \mathcal{C}_{44,0}$	Elastic constants at 0K
m_{11}, m_{12}, m_{44}	Slopes of the temperature-dependent elastic constants
\mathbf{A}	Thermal expansion tensor
θ, θ_0	Current and reference absolute temperatures
μ, μ_0	Effective shear moduli at current temperature and 0K
$\mathbf{T}^e, \mathbf{P}, \mathbf{T}$	Elastic 2nd Piola stress, Piola stress, Cauchy stress
$\tau^\alpha, \tau_{eff}^\alpha$	Resolved shear stress, effective shear stress in slip system α
ΔG	Activation energy
k_B	Boltzmann's constant
p, q	Parameters for the shape of stress-dependent kink-pair formation energy
s_0	Far-field slip resistance
s^α	Slip resistance in slip system α
\tilde{s}_l, s_l	Temperature-dependent lattice resistance, lattice resistance at 0K
b	Magnitude of Burgers vector
$a^{\alpha\beta}$	Dislocation interaction matrix
ρ^α	Dislocation density in slip system α
\mathcal{L}^α	Mean free path of dislocation for slip system α
k_1, k_2	Mean free path coefficients
y_c^α, y_{c0}	Annihilation capture radius for slip system α , reference capture radius
A_{rec}	Capture radius energy
ρ	Material mass density
c	Specific heat
η	Taylor-Quinney factor

2 Single crystal behavior

2.1 Single crystal plasticity model

2.1.1 Kinematics

The deformation gradient is defined by,

$$\mathbf{F} = \text{Grad } \mathbf{y}, \quad (1)$$

where $\mathbf{y} = \boldsymbol{\varphi}(\mathbf{X}, t)$ is the spatial vector mapped via the motion, $\boldsymbol{\varphi}$ and \mathbf{X} is the material vector in the reference configuration. Here, “Grad” denotes a gradient in the reference configuration. The deformation gradient multiplicatively decomposes into its elastic (\mathbf{F}^e) and plastic (\mathbf{F}^p) parts,

$$\mathbf{F} = \mathbf{F}^e \mathbf{F}^p. \quad (2)$$

The spatial velocity gradient represents the rate of deformation in the deformed configuration by,

$$\mathbf{L} = \text{grad } \mathbf{v} = \dot{\mathbf{F}} \mathbf{F}^{-1}, \quad (3)$$

where \mathbf{v} is the spatial velocity field and “grad” is a gradient in the deformed configuration. The velocity gradient additively decomposes into elastic (\mathbf{L}^e) and plastic (\mathbf{L}^p) distortion rate tensors,

$$\mathbf{L} = \mathbf{L}^e + \mathbf{F}^e \mathbf{L}^p \mathbf{F}^{e-1}, \quad (4)$$

where $\mathbf{L}^e = \dot{\mathbf{F}}^e \mathbf{F}^{e-1}$ and $\mathbf{L}^p = \dot{\mathbf{F}}^p \mathbf{F}^{p-1}$. Rearranging Equation (4), we have,

$$\dot{\mathbf{F}}^p = \mathbf{L}^p \mathbf{F}^p \text{ with } \mathbf{F}^p(\mathbf{X}, 0) = \mathbf{1}. \quad (5)$$

The dislocation motion is assumed to take place throughout prescribed slip systems $\alpha = 1 \sim N$ in the lattice space. Here, we define the Schmid tensor $\mathbb{S}_0^\alpha = \mathbf{m}_0^\alpha \otimes \mathbf{n}_0^\alpha$, where \mathbf{m}_0^α is the slip direction and \mathbf{n}_0^α is the slip plane normal defined in the intermediate (or lattice) space elastically relaxed from the deformed spatial configuration. Since plastic flow takes place throughout the prescribed slip systems, the plastic distortion rate tensor in the lattice space is expressed by,

$$\mathbf{L}^p = \sum_{\alpha=1}^N \dot{\gamma}_p^\alpha \mathbb{S}_0^\alpha. \quad (6)$$

Here, $\dot{\gamma}_p^\alpha$ is the plastic shear strain rate in each of the slip systems. Equivalently, the rate of plastic distortion is expressed in the deformed configuration by,

$$\overline{\mathbf{L}^p} = \mathbf{F}^e \mathbf{L}^p \mathbf{F}^{e-1} = \sum_{\alpha=1}^N \dot{\gamma}_p^\alpha \mathbb{S}^\alpha, \quad (7)$$

where $\mathbb{S}^\alpha = (\mathbf{F}^e \mathbf{m}_0^\alpha) \otimes (\mathbf{F}^{e-T} \mathbf{n}_0^\alpha)$ is the Schmid tensor in the deformed configuration. Furthermore, plastic flow is incompressible since,

$$\text{tr} \mathbf{L}^p = 0. \quad (8)$$

The elastic deformation gradient allows for the polar decomposition,

$$\mathbf{F}^e = \mathbf{R}^e \mathbf{U}^e, \quad (9)$$

where \mathbf{R}^e is the elastic rotation and \mathbf{U}^e is the elastic right stretch. Then we define the elastic strain tensor as,

$$\mathbf{E}^e = \frac{1}{2}(\mathbf{C}^e - \mathbf{1}), \quad (10)$$

where $\mathbf{C}^e = \mathbf{F}^{eT} \mathbf{F}^e$ is the elastic right Cauchy-Green tensor. Thus, the elastic strain tensor is defined in the intermediate space.

2.1.2 Constitutive equations

The elastic free energy in the intermediate space is defined by,

$$\Phi = \Phi(\mathbf{E}^e, \theta) = \frac{1}{2} \mathbf{E}^e : \mathcal{C}[\mathbf{E}^e] - (\theta - \theta_0) \mathbf{A} : \mathcal{C}[\mathbf{E}^e]. \quad (11)$$

Here, “:” denotes the inner product of two tensors. Then, the elastic 2nd Piola stress conjugate to \mathbf{E}^e is obtained by,

$$\mathbf{T}^e = \frac{\partial \Phi(\mathbf{E}^e, \theta)}{\partial \mathbf{E}^e} = \mathcal{C}[\mathbf{E}^e - \mathbf{A}(\theta - \theta_0)], \quad (12)$$

where \mathcal{C} is the fourth order elastic stiffness tensor and \mathbf{A} is the second order thermal expansion tensor. Moreover, θ is the current absolute temperature and θ_0 is the reference temperature. The elastic 2nd Piola stress is related to the Piola stress \mathbf{P} by,

$$\mathbf{P} = \mathbf{F}^e \mathbf{T}^e \mathbf{F}^{p-T}. \quad (13)$$

Then, it is also related to the Cauchy stress \mathbf{T} , using the relation, $\mathbf{T} = J^{-1}\mathbf{P}\mathbf{F}^T$ with $J = \det\mathbf{F}$,

$$\mathbf{T}^e = J\mathbf{F}^{e-1}\mathbf{T}\mathbf{F}^{e-T}. \quad (14)$$

The resolved shear stress that drives slip on the α th slip system is projected from the elastic 2nd Piola stress via the Schmid tensor defined in the intermediate lattice space,

$$\tau^\alpha = \mathbf{C}^e\mathbf{T}^e : \mathbb{S}_0^\alpha \approx \mathbf{T}^e : \mathbb{S}_0^\alpha, \quad (15)$$

since the elastic deformation is small in this work.

The plastic strain rate in the α th slip system is then constitutively prescribed by the form of the thermally-activated velocity of screw dislocations,

$$\begin{aligned} \dot{\gamma}_p^\alpha &= \dot{\gamma}_0 \exp\left(-\frac{\Delta G}{k_B\theta} \left\langle 1 - \left(\frac{\tau_{eff}^\alpha}{\tilde{s}_l}\right)^p \right\rangle^q\right) \quad \text{for } \tau_{eff}^\alpha > 0, \\ \text{otherwise } \quad \dot{\gamma}_p^\alpha &= 0; \quad \tau_{eff}^\alpha = |\tau^\alpha| - s^\alpha, \end{aligned} \quad (16)$$

where τ_{eff}^α is the effective shear stress, $\dot{\gamma}_0$ is the reference slip rate, ΔG is the activation energy, k_B is Boltzmann's constant, s^α is the slip resistance from dislocation interaction, p and q denote the parameters for the shape of stress-dependent kink-pair formation energy, and $\langle \cdot \rangle = \frac{1}{2}(|\cdot| + (\cdot))$ is a Macaulay bracket. Furthermore, the temperature-dependent lattice resistance, \tilde{s}_l is expressed by,

$$\tilde{s}_l = s_l \frac{\mu}{\mu_0}, \quad (17)$$

where s_l is the lattice resistance at 0 K and $\mu_0 = \sqrt{C_{44,0} \left(\frac{C_{11,0} - C_{12,0}}{2} \right)}$ and $\mu = \sqrt{C_{44} \left(\frac{C_{11} - C_{12}}{2} \right)}$ are the effective shear moduli at 0K and current temperature, respectively.

2.1.3 Slip resistance and dislocation evolution

In classical crystal plasticity theories (Asaro 1983; Asaro and Needleman 1985; Kalidindi et al. 1992; Cuitiño and Ortiz 1993), the slip resistance s^α in each of the slip systems was taken to evolve according to a simple phenomenological model¹ that represents a first description of self- and latent-hardening in the slip systems. This simple phenomenological model was found to reasonably capture the strain-hardening behavior in bcc materials in various crystallographic

¹ $\dot{s}^\alpha = \sum_\beta h^{\alpha\beta} |\dot{\gamma}^\beta|$, where $h^{\alpha\beta}$ is the hardening matrix.

orientations (Yalcinkaya et al. 2008; Cho et al. 2018). More recently, many single crystal plasticity models for both fcc and bcc materials have employed a modified Taylor hardening law associated with the evolution of dislocation densities (Bronkhorst et al. 2019; Lim et al. 2020; Nguyen et al. 2021). In this work, we employ the modified Taylor hardening law to better represent the underlying physics for the evolution of dislocations and their interactions throughout the slip systems. The slip resistance in the α -th slip system is expressed as,

$$s^\alpha = s_0 + \mu b \sqrt{\sum_{\beta=1}^N a^{\alpha\beta} \rho^\beta}, \quad (18)$$

where s_0 is the far-field resistance to slip, μ is the effective shear modulus, b is the magnitude of Burgers vector and ρ^β is the dislocation density in each slip system, β . Moreover, $a^{\alpha\beta}$ is the interaction matrix that characterizes the interaction strength between the slip systems α and β , which will be further discussed below.

In order to compute the slip resistance in the modified Taylor hardening law (Equation (18)), the dislocation density in each of the slip systems must be simultaneously computed via an appropriate evolution model. Numerous evolution models for computing the dislocation density exist in the literature for single crystal plasticity theories of bcc materials. Some bcc single crystal plasticity models have used a simple evolution rule for dislocation densities in which the interaction strengths between the slip systems were assumed to be equal (Knezevic et al. 2014; Lim et al. 2015b), following the classical work by Kocks 1976. Moreover, there is vast literature on the bcc single crystal plasticity models in which the geometric features in dislocation interactions throughout the slip systems were taken into account. Ma and Roters 2004 and Ma et al. 2007 proposed a simple model in which the forest and parallel dislocation densities associated with the slip resistance in a slip system (α) were computed such that dislocation densities in all other slip systems ($\beta \neq \alpha$) were geometrically projected onto the central slip system (α). Their interpretation for geometry of dislocation interaction was recently employed to model single crystalline bcc tungsten (Cereceda et al. 2016) exhibiting anomalous yield features due to non-Schmid effects. More recently, Nguyen et al. 2021 modified the geometric interaction model of Ma, Roters and Raabe to account for evolution of forest and co-planar (including parallel) dislocation densities in which the mixed characteristics of edge and screw dislocations were taken into account. All of these models have found success in capturing some important features in the thermomechanical behavior of single crystal bcc materials in various crystallographic ori-

entations. Yet, these models for bcc single crystal plasticity have limitation in accounting for the dislocation density evolution associated with interaction strengths strongly dependent on the type of interaction as well as the dependence of the dislocation interaction strengths on the hardening behavior. Single crystal plasticity model for bcc materials needs to be further extended in order to more accurately account for the hardening behavior associated with the dislocation microstructure, interaction and generation throughout the slip systems.

Meanwhile, mesoscopic dislocation dynamics (dd) simulations have enabled computing the interaction properties of dislocations for which both short-range contact interactions and long-range elastic interactions are taken into account throughout the slip systems for single crystalline fcc (Madec et al. 2003; Devincre et al. 2006) and bcc materials (Queyreau et al. 2009; Madec and Kubin 2017). Specifically, for both fcc and bcc crystals, the dd simulations have elucidated the roles of collinear interactions and various junctions in the slip activation processes as well as the hardening mechanisms throughout slip systems, as well postulated in Madec et al. 2003 and Devincre et al. 2005. Hence, a “soft” multi-scaling between the mesoscopic dd simulation and the macroscopic hardening law has enriched the physical picture in the continuum single crystal models in which the dislocation interaction strengths are explicitly taken into account (Dequiedt et al. 2015; Bronkhorst et al. 2019). In this work, we employ dd simulation results for tantalum to better represent the dislocation microstructures and interactions in our single crystal model.

The dislocation density in each of the slip systems in Equation (18) is taken to evolve according to a multiplication-annihilation type model (Dequiedt et al. 2015),

$$\dot{\rho}^{\alpha} = \frac{1}{b} \left(\frac{1}{\mathcal{L}^{\alpha}} - 2y_c^{\alpha} \rho^{\alpha} \right) |\dot{\gamma}_p^{\alpha}| \quad (19)$$

where \mathcal{L}^{α} is the mean free path of dislocations, and y_c^{α} is the annihilation capture radius. The mean free path is inversely proportional to the forest dislocation density, i.e.,

$$\frac{1}{\mathcal{L}^{\alpha}} = \sqrt{\sum_{\beta=1}^N d^{\alpha\beta} \rho^{\beta}} \quad (20)$$

with $d^{\alpha\beta} = \frac{a^{\alpha\beta}}{k_1}$ for self interaction or coplanar interaction, and $d^{\alpha\beta} = \frac{a^{\alpha\beta}}{k_2}$ for other interactions, where k_1 and k_2 are the mean free path coefficients. In this work, we employ the interaction strengths, $a^{\alpha\beta}$, informed by dd simulations for tantalum recently performed by Madec and

Kubin 2017. Further detailed description of the dislocation interaction strengths employed in our model is provided together with other material parameters in Section 2.1.5. Moreover, the temperature and rate-dependent annihilation capture radius is expressed by,

$$y_c^\alpha = y_{c0} \left(1 - \frac{k_B \theta}{A_{rec}} \ln \left| \frac{\dot{\gamma}_p^\alpha}{\dot{\gamma}_0} \right| \right), \quad (21)$$

where y_{c0} is the reference annihilation capture radius, and A_{rec} is the capture radius energy, following Beyerlein and Tomé 2008.

2.1.4 Temperature evolution

It has been known that during plastic deformation of metallic materials, the plastic work is partitioned into stored energy of cold work and thermal energy (Bever et al. 1973; Farren and Taylor 1925; Taylor and Quinney 1934; Titchener and Bever 1958). The energy stored in the atomic bond extension and contraction due to the evolution of dislocation density and structure is significant. The proportion of plastic work partitioned into thermal energy is generally termed the Taylor-Quinney factor (Taylor and Quinney 1934). Although it has been demonstrated that the Taylor-Quinney factor is very likely not constant and can take values substantially below 1.0 (Dorogoy and Rittel 2017; Lieou and Bronkhorst 2020; Lieou and Bronkhorst 2021; Rittel et al. 2012; Rittel et al. 2017), doing so within the present structural theory is beyond the scope of this work and therefore is assumed to simply remain constant. The evolution of temperature is then taken as

$$\rho c \dot{\theta} = \eta \sum_{\alpha=1}^N \tau^\alpha \dot{\gamma}_p^\alpha, \quad (22)$$

where η is the Taylor-Quinney factor, ρ is the material mass density, and c is the specific heat. Furthermore, it is assumed for strain rates below 1000 s^{-1} that $\eta = 0.0$ and above that $\eta = 1.0$. The Laplacian term in the original heat equation has also been neglected.

2.1.5 Slip systems and material parameters

As noted in the introduction, screw dislocations in tantalum and other bcc metallic materials dissociate into non-planar partial dislocation configurations while at rest as a lower energy state. This creates ambiguity in the proper stress to use to drive dislocation motion as the partial dislocation configuration is believed to be composed of three Burgers vectors which form a triangle. To provoke motion of screw dislocations, the split core must be forced to become planar once again and given the triangular configuration of the partial dislocations, the stress conditions to do so are not directionally isotropic and set up a condition of twin and anti-twin directionality

Table. 2. Slip systems for $\{110\}\langle 111 \rangle$

Slip system	\mathbf{m}_0^α	\mathbf{n}_0^α
A2	$[\bar{1}11]$	$(0\bar{1}1)$
A3	$[\bar{1}11]$	(101)
A6	$[\bar{1}11]$	(110)
B2	$[111]$	$(0\bar{1}1)$
B4	$[111]$	$(\bar{1}01)$
B5	$[111]$	$(\bar{1}10)$
C1	$[\bar{1}\bar{1}1]$	(011)
C3	$[\bar{1}\bar{1}1]$	(101)
C5	$[\bar{1}\bar{1}1]$	$(\bar{1}10)$
D1	$[1\bar{1}1]$	(011)
D4	$[1\bar{1}1]$	$(\bar{1}01)$
D6	$[1\bar{1}1]$	(110)

Table. 3. Slip systems for $\{112\}\langle 111 \rangle$

Slip system	\mathbf{m}_0^α	\mathbf{n}_0^α
A <u>4</u>	$[\bar{1}11]$	(211)
A <u>8</u>	$[\bar{1}11]$	$(\bar{1}1\bar{2})$
A <u>11</u>	$[\bar{1}11]$	$(\bar{1}21)$
B <u>3</u>	$[111]$	$(\bar{2}11)$
B <u>7</u>	$[111]$	$(11\bar{2})$
B <u>12</u>	$[111]$	$(1\bar{2}1)$
C <u>2</u>	$[\bar{1}\bar{1}1]$	$(\bar{1}\bar{1}2)$
C <u>5</u>	$[\bar{1}\bar{1}1]$	$(\bar{1}21)$
C <u>10</u>	$[\bar{1}\bar{1}1]$	$(2\bar{1}1)$
D <u>1</u>	$[1\bar{1}1]$	$(1\bar{1}2)$
D <u>6</u>	$[1\bar{1}1]$	(121)
D <u>9</u>	$[1\bar{1}1]$	$(\bar{2}\bar{1}1)$

for the motion of these dislocations on any given slip system. Atomistic calculations of screw dislocation dissociation in a number of different bcc materials on the $\{110\}\langle 111 \rangle$ type of systems has been clearly demonstrated (Duesbery et al. 1973; Gröger et al. 2008a; Gröger et al. 2008b; Yang et al. 2001). Similar demonstration for the $\{112\}\langle 111 \rangle$ and $\{123\}\langle 111 \rangle$ types has not yet been made. Neither has the influence of the split dislocation core upon dislocation interactions been studied in bcc metals given the hypothesis that screw dislocation motion may be via the nucleation and propagation of kink-bands (Butler et al. 2018). We know from prior work that including both $\{110\}\langle 111 \rangle$ and $\{112\}\langle 111 \rangle$ types of slip systems as options for dislocation motion is necessary to properly describe crystallographic texture evolution (Bronkhorst et al. 2006; Kothari and Anand 1998) with the role of $\{123\}\langle 111 \rangle$ systems within a continuum crystal mechanics setting unclear. Although, not yet well quantified, there are indications that the directional asymmetry described above is reduced with increase in material temperature (Lim et al. 2015a). Prior work has estimated this to be noticeable but small at room temperature for tantalum (Bronkhorst et al. 2021; Cho et al. 2018). Therefore, given the current uncertainties presented, we employ the traditional Schmid tensor and corresponding resolved shear stress as the primary external driving force for dislocation motion on the $\{110\}\langle 111 \rangle$ and $\{112\}\langle 111 \rangle$ types and treat all slip systems equally. Slip systems are listed in Table 2 and 3.

The material parameters used in the model are listed in Table 4. The mass density ρ , specific

Table. 4. Material parameters used in this study

ρ [kg/m ³]	16640	a_J	0.05
c [J/kg-K]	150	a_{XJ}	0.04
α [μ m/m-K]	6.5	s_0 [MPa]	35.0
k_b [J/K]	1.38×10^{-23}	$\dot{\gamma}_0$ [sec ⁻¹]	1.0×10^7
$C_{11,0}$ [GPa]	268.5	ΔG [J]	2.1×10^{-19}
$C_{12,0}$ [GPa]	159.9	s_l [MPa]	400.0
$C_{44,0}$ [GPa]	87.1	$\sum_{\alpha} \rho_0^{\alpha}$ [m ⁻²]	2.4×10^{12}
m_{11} [MPa/K]	-24.5	y_{c0}	$6b$
m_{12} [MPa/K]	-11.8	A_{rec} [J]	2.0×10^{-20}
m_{44} [MPa/K]	-14.9	p	0.28
a_{copl}	0.06	q	1.34
$a_{colli\ 60^\circ}$	0.7744	k_1	180
$a_{colli\ 90^\circ}$	0.9025	k_2	2.5
$a_{colli\ 30^\circ}$	0.5112	b [nm]	0.286

heat c , and thermal expansion tensor $\mathbf{A} = \alpha \mathbf{1}$ are assumed to be constant during deformation. The fourth order elastic stiffness tensor is expressed in terms of the three independent elastic constants (\mathcal{C}_{11} , \mathcal{C}_{12} , \mathcal{C}_{44}). The elastic constants are linearly dependent on temperature as $\mathcal{C}_{ij} = \mathcal{C}_{ij,0} + m_{ij}\theta$. $\{\mathcal{C}_{11,0}, \mathcal{C}_{12,0}, \mathcal{C}_{44,0}\}$ at 0 K and $\{m_{11}, m_{22}, m_{33}\}$ are assumed to follow the previous work by Kothari and Anand 1998, Cho et al. 2018 and Bronkhorst et al. 2021. The values of $\dot{\gamma}_0$, ΔG , s_l and p and q in the flow model are identified based on the previous work that employed similar single crystal models for tantalum (Kothari and Anand 1998; Cho et al. 2018; Bronkhorst et al. 2021). Then, these values have been further tuned to better capture the rate-dependent stress-strain behaviors in the single crystals.

The dislocation interaction coefficients are taken to follow the work by Madec and Kubin 2017. Instead of using the full asymmetric interaction matrices throughout the slip systems of $\{110\}\langle 111 \rangle$ and $\{112\}\langle 111 \rangle$, we further simplified the interaction coefficients, as follows.

- $a_{\text{copl}} = 0.06$ for the self- and coplanar interactions (Dequiedt and Denoual 2021),
- $a_{\text{colli } 60^\circ} = 0.7744$ for the collinear interaction and $\theta = \arccos|\mathbf{n}_0^\alpha \cdot \mathbf{n}_0^\beta| = 60^\circ$,
- $a_{\text{colli } 90^\circ} = 0.9025$ for the collinear interaction and $\theta = \arccos|\mathbf{n}_0^\alpha \cdot \mathbf{n}_0^\beta| = 90^\circ$,
- $a_{\text{colli } 30^\circ} = 0.5112$ for the collinear interaction and $\theta = \arccos|\mathbf{n}_0^\alpha \cdot \mathbf{n}_0^\beta| = 30^\circ$,
- $a_J = 0.05$ for the junctions between $\{110\}$ systems or $\{112\}$ systems,
- $a_{XJ} = 0.04$ for the junctions between $\{110\}$ and $\{112\}$ systems.

As pointed out in Monnet and Devincere 2006, the presence of the friction stress due to alloy friction or lattice resistance can screen the elastic field between dislocations. Thus, this culminates in a decrease in the line-tension and interaction strengths. Since the lattice resistance has been taken into account in our single crystal model, the values for the junction strengths (a_J, a_{XJ}) are taken to be smaller than the average junction strengths determined in Madec and Kubin 2017.

The values for the remaining parameters, s_0 , y_{c0} , A_{rec} , k_1 , and k_2 are then identified using the experimental data for the single crystal behaviors at low to high strain rates and for the polycrystal behavior at low strain rate in through-thickness direction.

2.2 Results: experiment vs. model

The finite deformation single crystal model presented in Section 2.1 was numerically implemented for use in a finite element solver (a standard branch of Abaqus) for boundary value problems of single- and polycrystalline tantalum discussed in the next sections. We implemented

the implicit multi-step computational procedure for updating the stress tensor, kinematic tensors and all of the state variables including the dislocation densities evolving together with deformation, following and modifying the algorithms proposed by Kalidindi et al. 1992 and Anand 2004. Furthermore, we computed a forth order tangent tensor also known as the Jacobian consistent with the viscoplastic single crystal model used in a Newton-type iteration for obtaining a solution that satisfies the global equilibrium at the end of the increment in the nonlinear boundary value problems, based on the procedures detailed in Dai 1997 and Balasubramanian 1998. All the details regarding the implicit time integration procedure and the computation of tangent are provided in the Appendices A and B, respectively.

Here, we validate the finite deformation single crystal model presented above against experimental data for single crystal tantalum. We used the single crystal stress-strain data at low to high strain rates recently published by Nguyen et al. 2021, Rittel et al. 2009 and Whiteman et al. 2019.

2.2.1 Single crystal behavior at low to high strain rate

Figure 1 shows the measured and numerically simulated stress-strain curves for single crystalline tantalum in crystallographic orientations of $[001]$, $[01\bar{1}]$, $[111]$ and $[\bar{1}49]$ at strain rates of 0.001 s^{-1} and 0.1 s^{-1} . As evidenced in the figures, the model captures well the main features of the rate-dependent yield and flow stresses for the various crystallographic directions. The highest initial yield point and the flow stresses in the $[111]$ orientation due to the lowest Schmid factor are nicely described in the model. Furthermore, the hardening behavior and its tendency towards larger strains are reasonably captured in the $[001]$, $[111]$ and $[\bar{1}49]$ orientations. However, in the $[01\bar{1}]$ orientation, the hardening behavior observed in the experiment is poorly predicted by the model. This discrepancy can likely be attributed to crystallographic misorientation² or some finite size effects in samples during experimentation. Additionally, the stress-strain behavior in this particular $[01\bar{1}]$ orientation has large variations amongst the experimental data reported by different research groups (Rittel et al. 2009; Lim et al. 2020; Whiteman et al. 2019).

In Figure 2, the single crystal behavior is further presented at high strain rates in both experiments and numerical simulations. The high strain rate curves are displayed for room temperature and higher in the crystallographic orientations of $[001]$ (Figure 2a), $[01\bar{1}]$ and $[111]$

²As pointed out by Cuitiño and Ortiz 1993 and Stainier et al. 2002, for single crystal specimens with high symmetric orientation along the loading direction, small misalignment in the loading axis breaks the symmetry of resolved shear stress, resulting in a significant change in slip activity and stress responses.

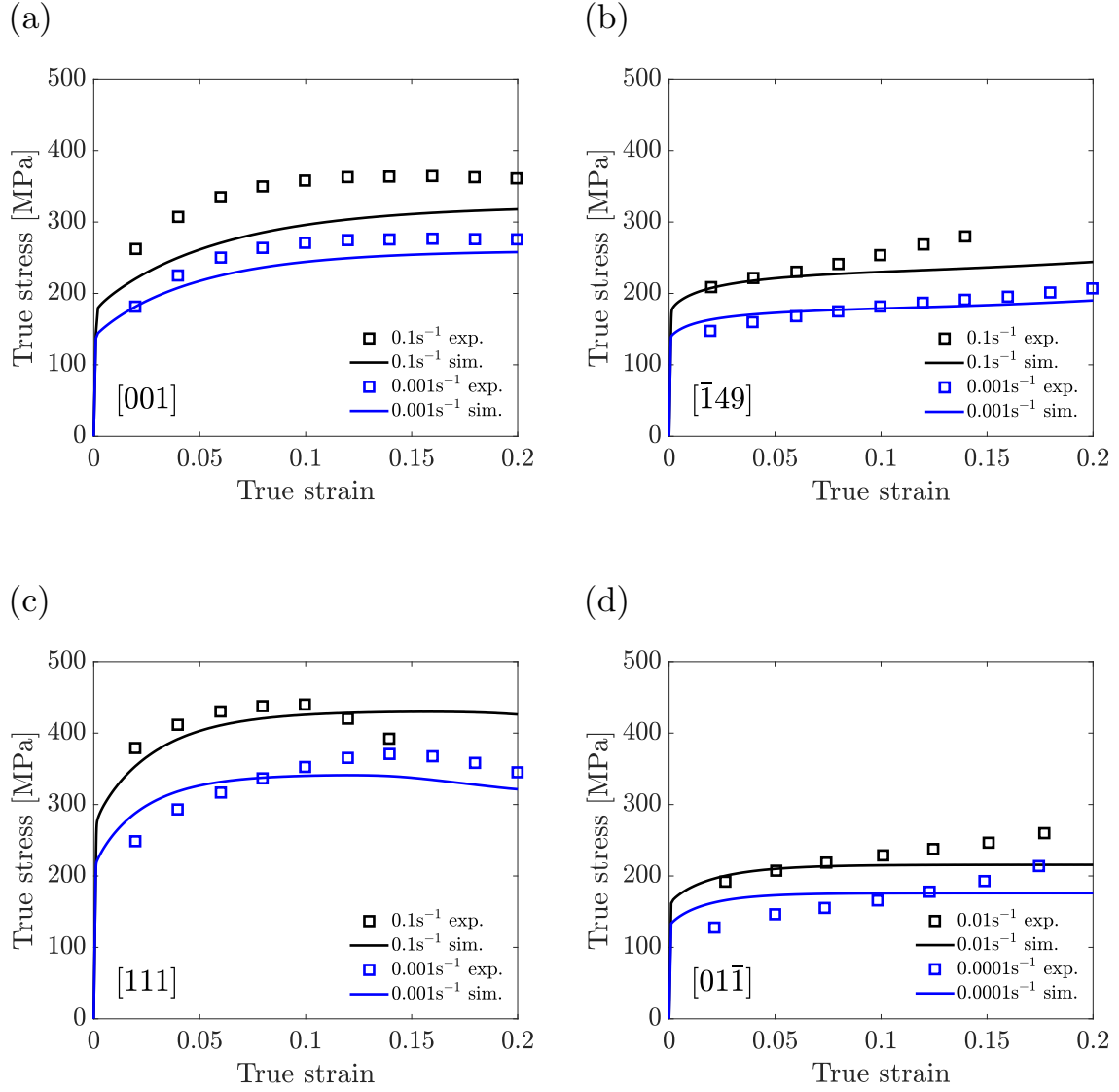


Figure. 1. Stress-strain behavior of single crystal tantalum in experiments and numerical simulations at low strain rates: (a) [001], (b) $[1\bar{4}9]$, (c) [111] and (d) $[01\bar{1}]$ in compression. The single crystal data were taken from Lim et al. 2020 and Rittel et al. 2009.

(Figure 2b). The orientation- and temperature-dependent yield stress and flow stresses are excellently captured by the model. Furthermore, the single crystal model captures nicely the thermal softening that manifests due to adiabatic heating under high strain rate conditions. In summary, our single crystal model has been shown to be capable of capturing the main features of the orientation-dependent stress-strain behaviors of single crystal tantalum at low (0.001 s^{-1}) to high ($\sim 5000 \text{ s}^{-1}$) strain rates and at room (296K) to high (873K) temperatures.

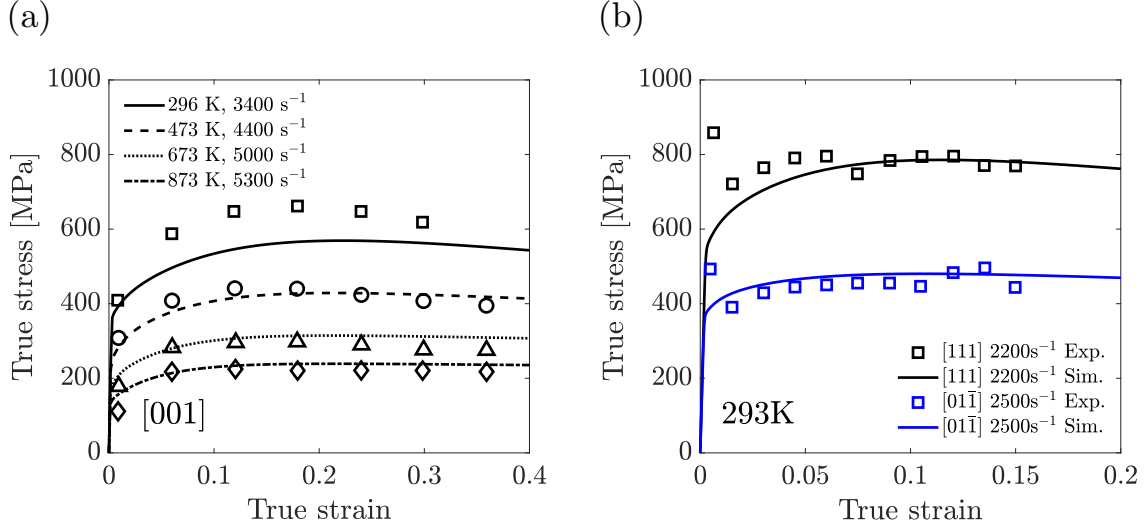


Figure. 2. Stress-strain behavior of single crystal tantalum in experiments (open symbols) and numerical simulations (lines) at high strain rate compression. (a) [001] at room temperature to higher (b) [011] and [111] at high strain rates. The single crystal data were taken from Nguyen et al. 2021 and Whiteman et al. 2019.

2.2.2 Effects of collinear interactions on slip activity and instability in single crystals

The collinear interactions taken into account in our single crystal model have been found to be of critical importance for predicting active slip systems in single crystals loaded in orientations with high symmetry (e.g. $\langle 100 \rangle$ and $\langle 110 \rangle$), as posited by Madec et al. 2003 and Devincre et al. 2005. Devincre et al. 2005 also reported on important experimental results for fcc single crystals loaded in the $\langle 100 \rangle$ orientation. In their experiment, though eight primary slip systems had the same Schmid factor, only four of them were found to be activated under deformation, attributed to instability induced by the strong collinear interactions between the eight slip systems; i.e., only one in a collinear pair of two slip systems was found to be activated for slip. Here, we analyze the role of collinear interactions in the slip activation processes for this exemplar tantalum single crystal. We also numerically examine instability induced by strong collinear interactions, especially on $\{110\}$ slip planes. Towards this end, we excluded the 12 $\{112\}$ $\langle 111 \rangle$ slip systems in the numerical simulations for single crystals ³.

Figure 3 shows a numerically simulated stress-strain response in a tantalum single crystal loaded in a high symmetry orientation of $\langle 100 \rangle$, together with accumulated slips and slip re-

³If the $\{112\}$ slip systems are included, no slip systems in collinear interactions are activated in single crystal samples loaded in the high symmetry orientations of $\langle 100 \rangle$, $\langle 110 \rangle$ and $\langle 111 \rangle$. Hence, no instability is observed as shown in our results in Figure 1 and 2.

sistances in eight slip systems having the same Schmid factor. Here, (A3, A2), (B4, B2), (C3, C1) and (D4, D1) are the pairs of slip systems collinear-interacting on the $\{110\}$ slip planes. As shown in Figure 3b, initially, though the accumulated slips in these eight slip systems evolve at the same rate, they bifurcate after a small amount of deformation. Interestingly, in the deactivated cross-slip systems (A3, B4, C3 and D4), the slip resistance continues to evolve. While, in the active slip systems (A2, B2, C1 and D1), it does not evolve significantly since their cross-slip counterparts become deactivated (See the modified Taylor hardening law in Equation (18)). The instability in the slip activation process was found to culminate in an anomalous stiff response beyond the initial yield as shown in Figure 3a (black solid line with no misorientation). Such an anomalous stress response sustains until the collinear interactions vanish due to the lattice distortion in the deformed single crystal. Next, we introduced a slight misorientation (0.6°) between the sample axis and the loading direction. The slight misorientation resulted in asymmetry in the initial Schmid factors (or resolved shear stresses) for the eight slip systems. The asymmetry due to the slight misorientation culminated in early determination for activation throughout the slip systems. Hence, as evidenced in the simulated stress-strain curve (red solid line in Figure 3a), the abnormally stiff response observed in the perfectly oriented sample diminishes significantly with misorientation.

The single crystal response in this high symmetry orientation is further examined with a weaker collinear interaction strength. As shown in Figure 3c, the single crystal exhibits a stress-strain behavior without any precursor for instability. Such a stable hardening behavior is clearly evidenced by Figure 3d on slip resistances and accumulated slips in the eight slip systems. These slip systems having the same Schmid factor are equally active without any bifurcation during deformation. These results strongly support the idea that the collinear interactions play a critical role in determining slip activation processes in bcc single crystals loaded in high symmetry orientations. It should be noted that the slip activation mechanisms as well as the instability phenomena cannot be accounted for by the early bcc single crystal models with the phenomenological hardening law or the modified Taylor hardening law without any notion of collinear interactions informed by the mesoscopic dislocation dynamics simulations. It should also be noted that the instability induced by the strong collinear interactions is particularly important in analyzing the bcc single crystal behavior where slips on the $\{110\}$ planes are more likely to be activated (e.g. Cho et al. 2018; Lim et al. 2015b; Narayanan et al. 2014; Patra et al. 2014).

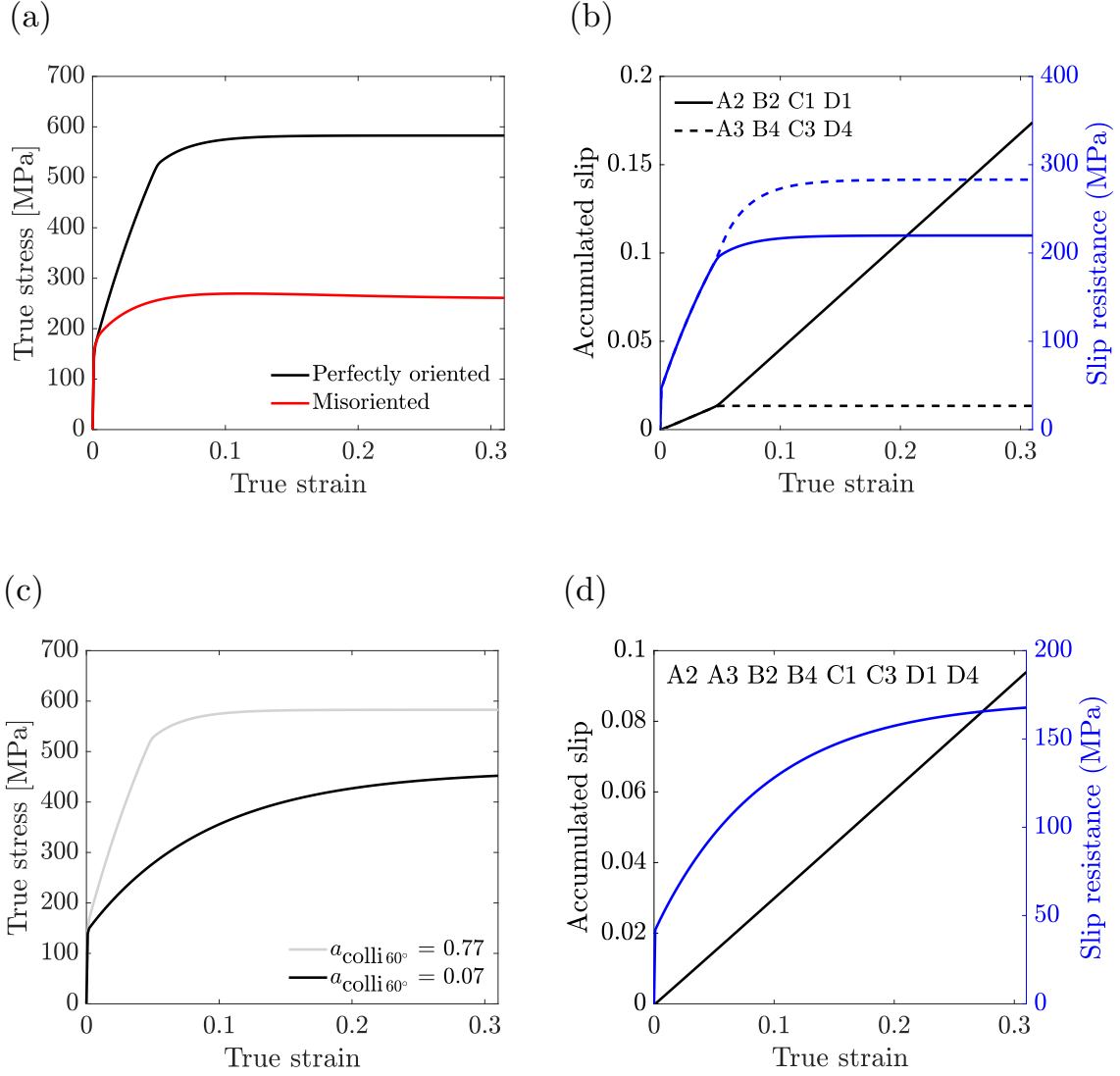


Figure. 3. Effect of collinear interactions on single crystal behavior loaded in high symmetry orientations. (a) Stress-strain curves with and without misorientation, (b) evolution of accumulated slip and slip resistance without misorientation, (c) stress-strain curves and (d) accumulated slip and slip resistance with a weaker collinear interaction.

3 Polycrystal behavior

The deformation mechanisms in polycrystal tantalum have been investigated, traced back to the early work by Hoge and Mukherjee 1977, Chen and Gray 1996, Nemat-Nasser et al. 1998 and Kothari and Anand 1998. In these classical papers, the highly temperature- and rate-dependent inelastic features in polycrystal tantalum were addressed. Furthermore, the polycrystal models that employed the phenomenological hardening law was found to capture well some features in flow stresses and crystallographic texturing without any notion on dislocation evolution and interaction. This success with the phenomenological hardening law has been deemed due to

the macroscopic hardening responses not sensitive to the details of dislocation evolution and interaction throughout the polycrystalline network.

Here, the single crystal model presented in the Section 2 is further underpinned by examining the predictive capabilities of the model for polycrystal tantalum. To this end, we conducted mechanical tests for polycrystal tantalum samples machined in two different directions (through-thickness and in-plane) taken from the wrought tantalum plate. Furthermore, *ex situ* measurements on crystallographic texture evolution in the deformed samples at increasing strains were conducted. In addition to crystallographic texture, dislocation density was monitored using *ex situ* neutron diffraction measurements. The polycrystalline behavior involving stress-strain responses, dislocation density evolution and texture evolution is then reproduced in numerical simulations in which the single crystal plasticity model is employed without any further modification. The results below show the predictive capabilities of our modeling framework on both single- and polycrystal tantalum materials at low to high strain rate and at room temperature and higher.

3.1 Experiment

Multiple cylindrical tantalum specimens of 4.2 mm diameter and 8.4 mm length were electro-discharge machined from a wrought plate with their axes parallel to either the through-thickness (TT) or in-plane (IP) directions. IP polycrystal tantalum specimens were compressed in-situ at a strain rate of 0.001 s^{-1} to maximum true strain levels of 0.08, 0.18, 0.44, 0.89 or 0.149. In parallel, the TT and IP specimens were compressed *ex situ* to compressive true strains of 0.2, 0.3 and 0.4.

Bulk texture measurements of the specimens were conducted on the High-Pressure/Preferred Orientation (HIPPO) neutron time-of-flight diffractometer (Wenk et al. 2003; Vogel et al. 2004) at the Lujan Center at the Los Alamos Neutron Science Center (LANSCE). HIPPO consists of 1,200 ^3He detector tubes on 45 panels arranged on five rings around the incident neutron beam with nominal diffraction angles of 144° , 120° , 90° , 60° , and 40° covering 22.4% of 4π (Takajo and Vogel 2018). The deformed samples at strains of 0.2, 0.3 and 0.4 were glued on to sample holders with their cylinder axis along the holder axis and loaded on an automated robotic sample changer on HIPPO (Losko et al. 2014). Data was then collected at three rotations around the sample axis of 0° , 67.5° , and 90° . Data over a d-spacing range from 0.7\AA to 2.5\AA was analyzed with the Rietveld method (Rietveld 1969) as implemented in the Materials Analysis

Using Diffraction (MAUD) code following procedures described previously (Wenk et al. 2010). The orientation distribution was represented by the E-WIMV method (Matthies et al. 2005) using a resolution of 7.5° . From the MAUD analysis, pole figure data recalculated from the refined ODF was exported for further processing.

High-resolution (FWHM $\sim 0.1\%$), high-statistics time-of-flight (TOF) neutron diffraction data was collected on the Spectrometer for MAterials Research at Temperature and Stress (SMARTS) for the purpose of diffraction line profile analysis (DLPA) (Brown et al. 2016) of each of the deformed specimens. The extended convolutional multiple whole profile (eCMWP) method (Ribárik et al. 2004) was used for semi-quantitative determination of the dislocation density in each of the deformed tantalum specimens. Annealed copper foil was used to determine the instrumental resolution and a Pearson VII function was used to fit the individual peak profiles to determine the breadth and shape parameters.

3.2 Results: experiment vs. numerical simulation

Numerical simulations for polycrystalline tantalum are conducted in which each of the finite elements represents one crystal. We use a finite element model comprising 1000 ($10 \times 10 \times 10$; Figure 4a) hexahedral elements with reduced integration. For simple compression, all faces are constrained to remain parallel, and displacement boundary conditions corresponding to loading conditions are applied on the top surface. The initial texture in each of the through-thickness and the in-plane direction was extracted from the measured data using MTEX (Bachmann et al. 2010) and the corresponding set of Euler angles (ϕ , θ and ω) was then randomly assigned to each of the elements in order to represent the initial material texture.

3.2.1 Stress-strain behavior, crystallographic texturing and dislocation density evolution

Figure 4 shows the response of polycrystal tantalum in compression (strain rate: 0.001 s^{-1}) in both experiment and numerical simulation. Together with undeformed and deformed meshes shown in Figure 4a, the measured and numerically simulated stress strain curves along the through-thickness direction are displayed in Figure 4b. As shown, the numerically simulated responses including yield stress and overall hardening behavior are in good agreement with the measured data.

Figures 5 and 6 shows a comparison of the pole figures from experiments and numerical

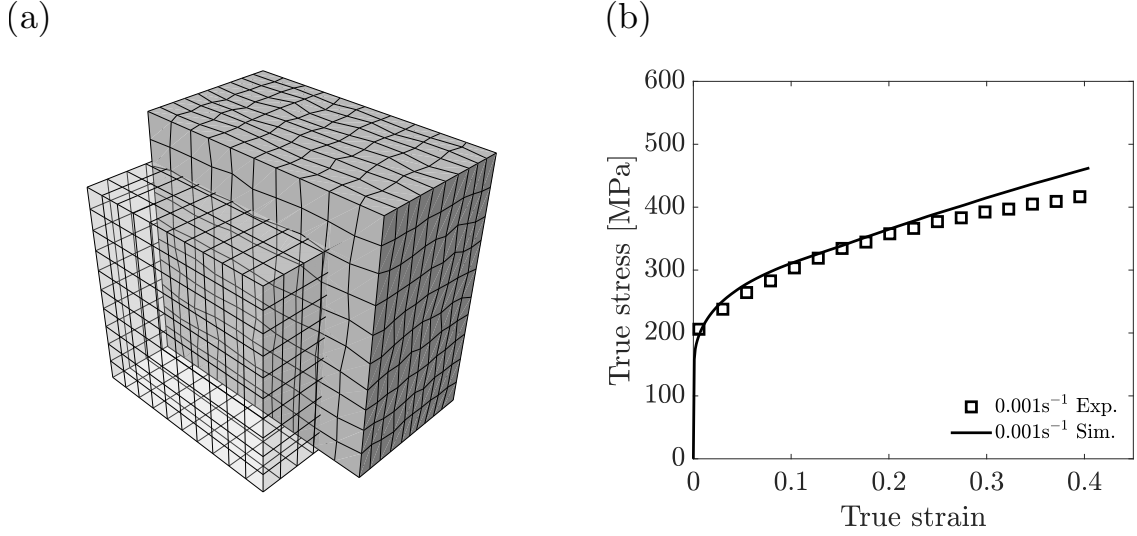


Figure. 4. (a) polycrystal model in undeformed (transparent) and deformed (gray) configurations, (b) stress-strain response in experiment and numerical simulation under loaded along the through-thickness direction at 0.001 s^{-1} and 300K.

simulations of the polycrystal tantalum under compression along the through-thickness and in-plane directions respectively. The sample in the through-thickness direction was found to be initially textured in the (100) and (111) as shown in Figure 5a at zero strain. In addition, the sample in the in-plane direction was found to be textured in the (110) direction as shown in Figure 6a at zero strain. The texture development toward the (100) and (111) directions is attributed to constrained rotations of grains by prescribed slip systems (Kocks et al. 1998), excellently predicted in our numerical simulations for both sample directions. Moreover, as recently pointed out in Lim et al. 2020 the rotation characteristics in bcc crystals are strongly dependent upon the types of the prescribed slip systems. Our experimental and numerical results on the texture evolution strongly support that the prescribed slip systems on both $\{110\}$ and $\{112\}$ planes have been appropriately chosen for this study.

We then directly compared the dislocation densities measured in our *ex situ* neutron diffraction experiments to those predicted in our numerical simulations in the through-thickness direction (Figure 7a) and the in-plane direction (Figure 7b). To this end, we plotted the flow stresses in the two sample directions as functions of dislocation density and imposed strain. Here, since the volume change is small, the total dislocation density is simply calculated by averaging the dislocation density at each integration point. As shown, our numerical simulations capture reasonably the relations between dislocation densities and macroscopic stress and strain

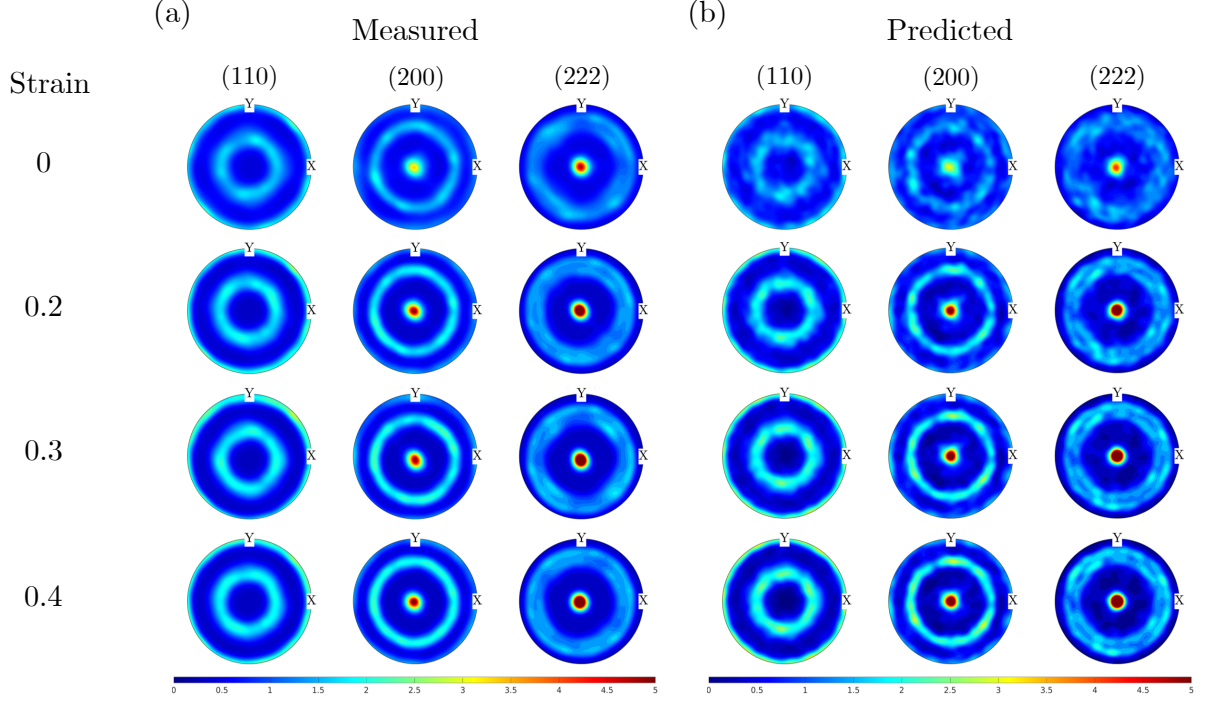


Figure. 5. Texture evolution during compression along the through-thickness direction. Pole figures (a) measured and (b) numerically predicted.

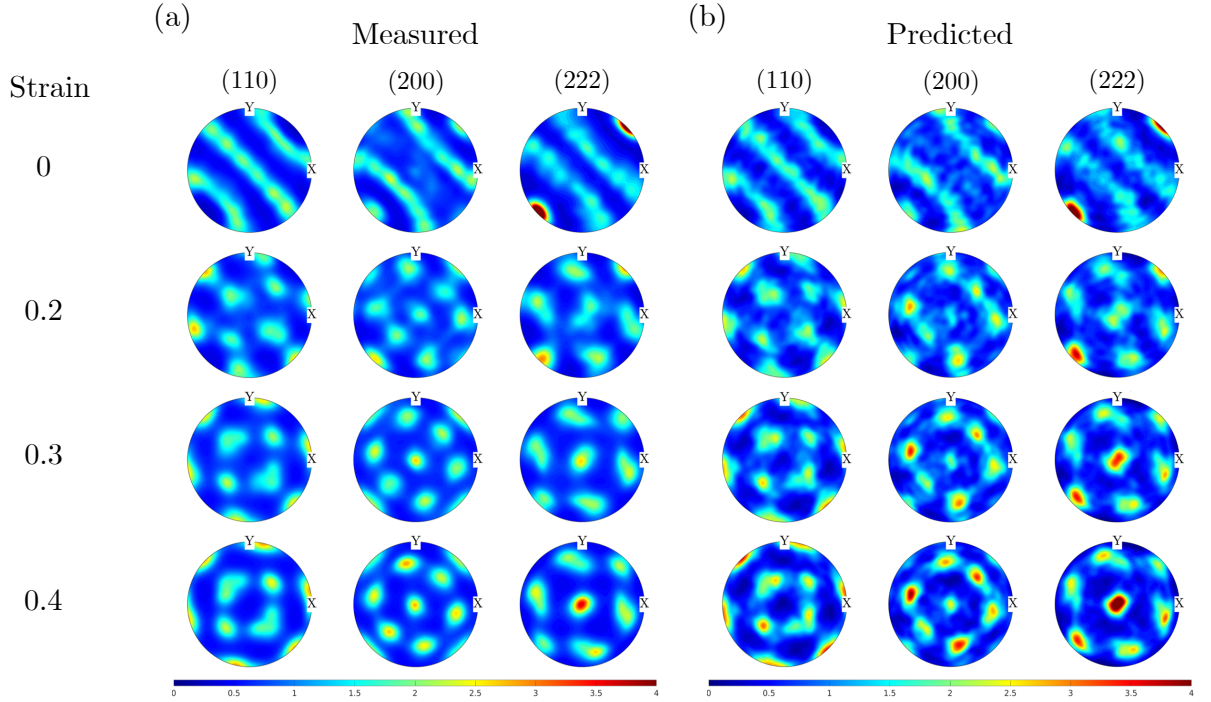


Figure. 6. Texture evolution during compression along the in-plane direction. Pole figures (a) measured and (b) numerically predicted.

responses in both sample directions in terms of trend. Furthermore, the flow stresses are linearly dependent on the square root of the averaged dislocation density in both experiments and numerical simulations. However, the overall stress response in the numerical simulation especially

in the in-plane direction is found to be higher than that in the experiment. This discrepancy is presumably attributed to a lack of information on initial distributions of dislocation densities for numerical simulations and not yet adequately representing the complexities of dislocation dynamics and intergranular interaction in the materials.

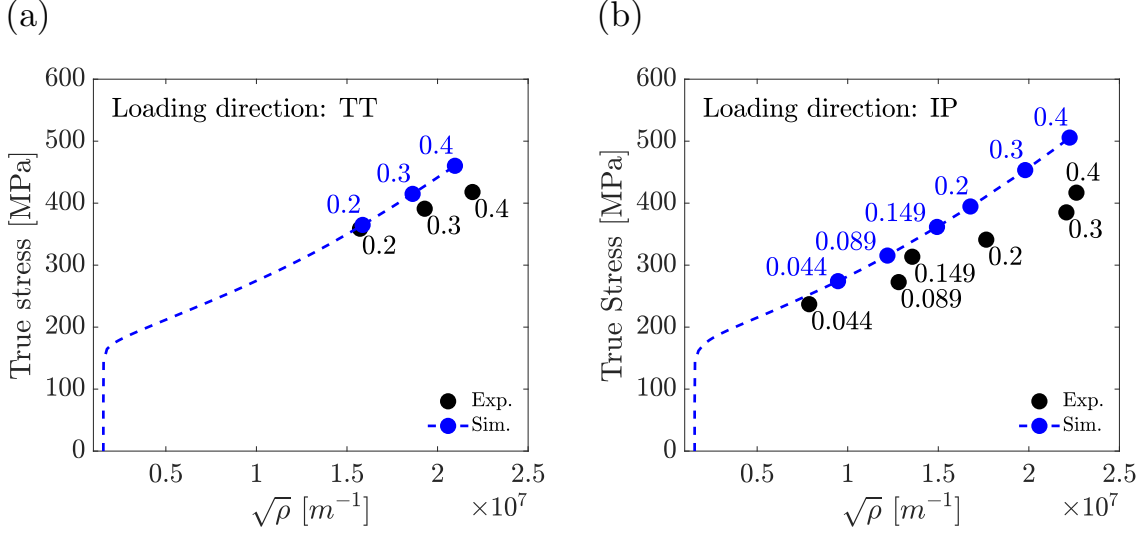


Figure. 7. Comparison between dislocation densities measured and numerically predicted for (a) through-thickness direction and (b) in-plane direction.

3.2.2 High strain rate and high temperature behavior

Figure 8 shows the stress-strain behavior of polycrystal tantalum in compression at higher temperature ($T \geq 298K$) and high strain rate ($\dot{\epsilon} > 10^3 s^{-1}$) in both experiments and numerical simulations. Here, the high strain rate data have been collected using a split Hopkinson pressure bar system. As shown in Figure 8a, the numerical simulations predict the low- to high strain rate behavior in polycrystal tantalum at room temperature reasonably well. Furthermore, the remarkable decreases in yield stress and flow stresses at higher temperatures of 473 K and 673 K are well captured in the numerical simulation displayed in Figure 8b and 8c. Although the overall high strain rate- and high temperature behavior is reasonably predicted, the high strain rate hardening features at room temperature and 473 K are poorly captured in the numerical simulations. It is presumably attributed to inaccuracy in the interaction properties computed from dd simulations especially at large strains and at high strain rates.

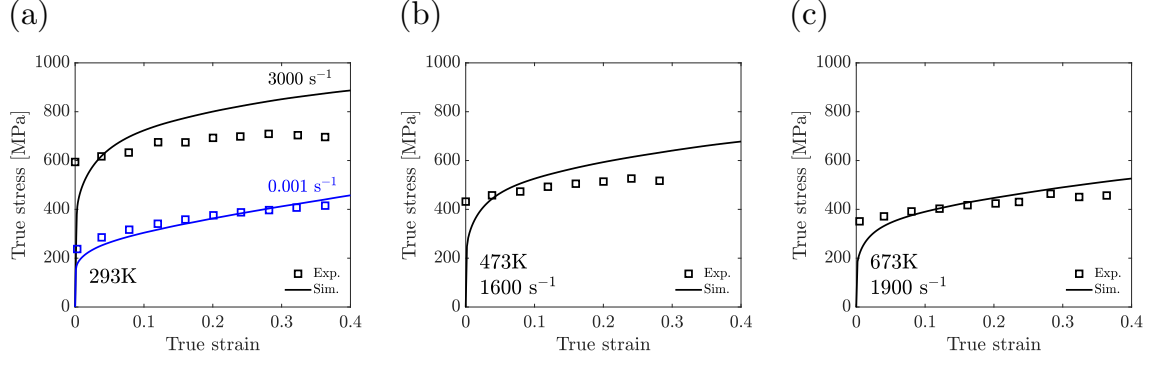


Figure. 8. Stress-strain behavior of polycrystal tantalum in experiments and numerical simulations at high strain rates and high temperatures: (a) at 298K 0.001 s^{-1} and 3000 s^{-1} , (b) at 473K 1600 s^{-1} , and (c) at 673K 1900 s^{-1} in compression.

3.3 Grain-level analysis for rotation and dislocation density evolution

The macroscopic features in dislocation density, crystallographic texturing and stress-strain responses in polycrystal tantalum samples have been found to be captured well by the simple polycrystal model in which each element represented one crystal. Here, the polycrystal behavior is further addressed by numerical simulations on a polycrystal model based on Voronoi-tessellation. Though this Voronoi-tessellation-based polycrystal model is not grain-boundary conforming, it enables analysis of the local variations of dislocation density, slip activity, stress and rotation throughout more realistic polycrystalline network not available in the simple polycrystal model presented in Section 3.2.

Figure 9a shows a Voronoi-tessellated unit-cube with 200 random spatial Voronoi points. The tessellated domain is meshed with the hexahedral elements via voxelization using an open-source program, Neper (Quey et al. 2011). Moreover, the number of random Voronoi points has been chosen such that the Voronoi model reproduces the texture evolution captured by the simple polycrystal model (the set of $10 \times 10 \times 10$ hexahedral elements) displayed in Figure 6. In the Voronoi-tessellation-based polycrystal model, each of the polyhedral Voronoi cells represents one crystal to which a set of Euler angles extracted from the experiment is assigned. Then we conducted numerical simulations for the polycrystal domains under large compression. As shown in Figure 9b, the macroscopic stress-strain curve in the Voronoi-tessellation-based polycrystal model matches well with that for the simple polycrystal model in the in-plane direction.

In the Voronoi-tessellation-based polycrystal model, three grains have been selected for detailed analysis for an intragranular behavior. The grain A initially oriented in the $[4\bar{1}9]$ direction

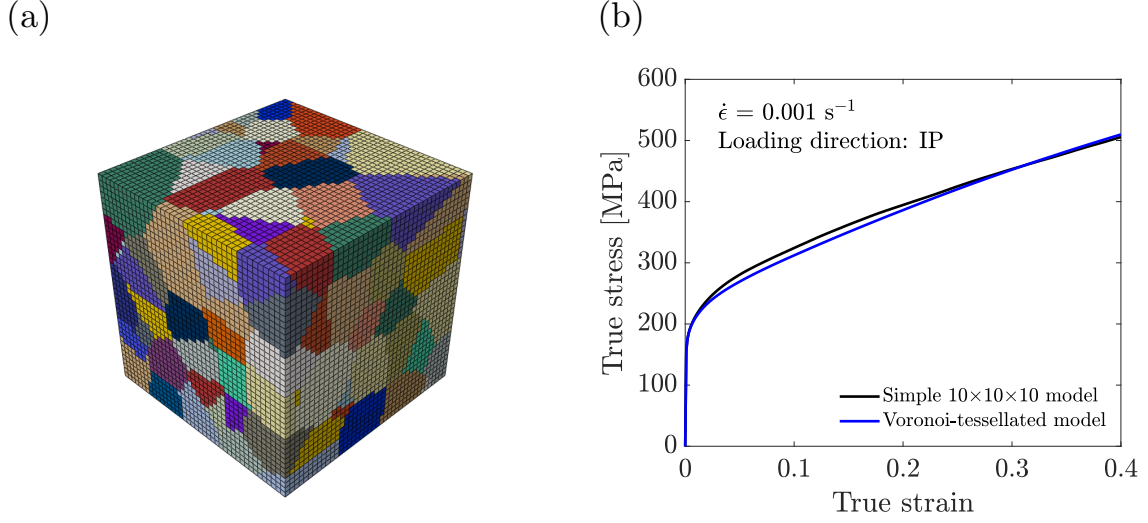


Figure. 9. (a) Voronoi-tessellation-based polycrystal model with 200 random spatial points (b) comparison of stress-strain curves between $10 \times 10 \times 10$ polycrystal model and Voronoi model in the in-plane direction.

was selected since the location in the standard triangle has the maximum Schmid factor on the $\{110\}$ slip planes (Figure 10a). Under deformation, as shown in Figure 10b, the grain tends to rotate toward the edge (between $[001]$ and $[\bar{1}\bar{1}1]$ of the standard triangle) and then toward $[001]$ such that the Schmid factor of the initially active slip system decreases along the corresponding great circle (Dieter and Bacon 1976). Furthermore, a significant variation in rotation (or intragranular orientation) is observed inside the grain, as shown in Figures 10b and 10c. Herein, the intragranular misorientation is computed via, $\Delta \mathbf{g}_i = \mathbf{g}_i \langle \mathbf{g}_{\text{avg}} \rangle^{-1}$, where $\Delta \mathbf{g}_i$ is the magnitude of misorientation between the orientation of a spatial intragranular point i (\mathbf{g}_i) and the average orientation in the grain (\mathbf{g}_{avg}), following Pokharel et al. 2014. Together with the intragranular rotation map, dislocation densities in major active slip systems at a strain of 0.4 are displayed in Figure 10d. Though the Schmid factor on the $\{110\}$ slip systems (e.g. the slip system of B2) is initially greater than on the $\{112\}$ slip planes, the dislocation densities are found to develop well on both $\{110\}$ and $\{112\}$ planes, due to the remarkable spatial variation in rotation inside the grain; i.e., at a strain of 0.4 (Figure 10c), the contour for local orientation in the grain A is widely located throughout the regions where the Schmid factors are strong on both $\{110\}$ and $\{112\}$ slip planes.

Then, a grain B initially oriented in the $[561]$ was selected since the initial orientation in the standard triangle has the maximum Schmid factor on the $\{112\}$ planes (Figure 11a). As shown in Figure 11b, the grain tends to rotate toward the $[111]$ direction such that the Schmid

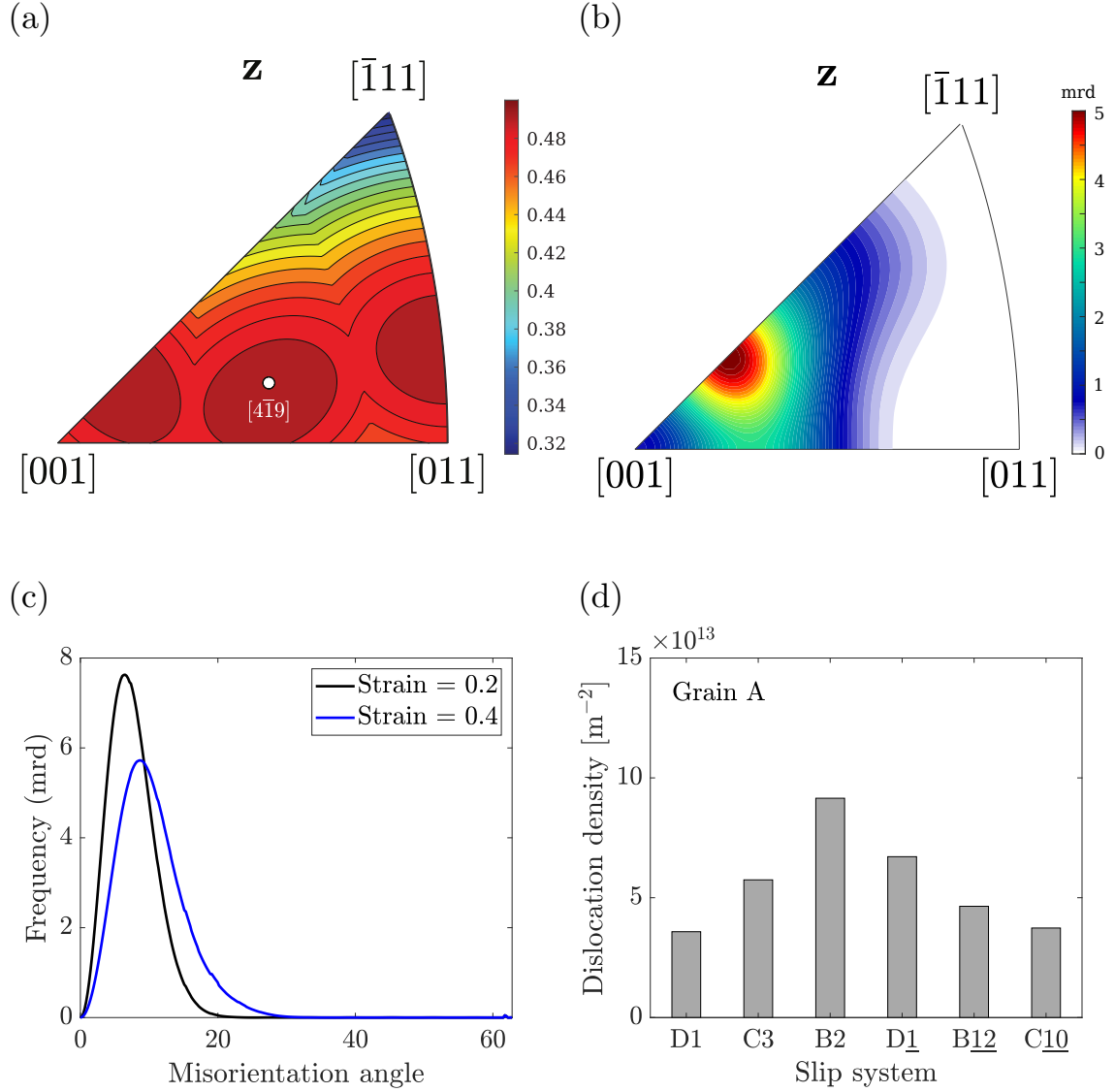


Figure. 10. Numerically predicted rotation and dislocation density in a grain A in the $[4\bar{1}9]$ direction within the Voronoi-tessellated polycrystal domain. (a) Location of the $[4\bar{1}9]$ direction on contour of the maximum Schmid factor, (b) countour of crystallographic orientations within the grain A at a strain of 0.4, (c) distribution of misorientation angle within the grain (strains of 0.2 and 0.4), (d) dislocation densities in slip systems on both $\{110\}$ and $\{112\}$ planes at a strain of 0.4.

factor decreases along the corresponding great circle. Moreover, once again a significant spatial variation in rotation is observed again in the grain B at increasing strains of 0.2 and 0.4, as displayed in Figure 11c. Dislocation densities in major active slip systems at a strain of 0.4 are also shown in Figure 11d. The dislocation density is found to grow remarkably, especially for a slip system on the $\{112\}$ plane (here, C $\bar{2}$). This is quite reasonable since the contour for local orientation in the grain B is still located in the region where the maximum Schmid factor is

incurred in the slip systems on the $\{112\}$ planes.

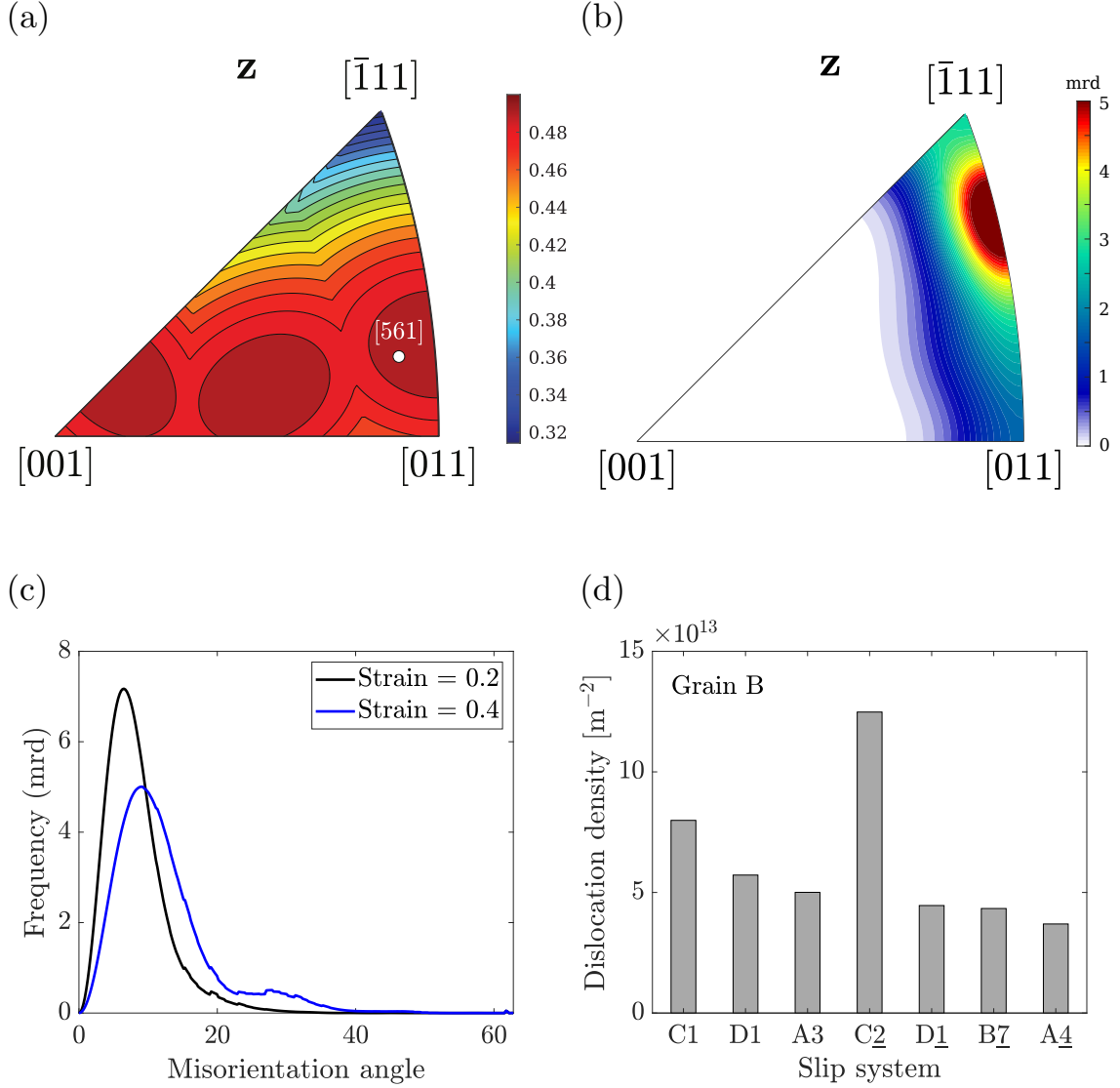


Figure. 11. Numerically predicted rotation and dislocation density in a grain B in the $[561]$ direction within the Voronoi-tessellated polycrystal domain. (a) Location of the $[561]$ direction on contour of the maximum Schmid factor, (b) countour of crystallographic orientations within the grain B at a strain of 0.4, (c) distribution of misorientation angle within the grain (strains of 0.2 and 0.4), (d) dislocation densities in slip systems on both $\{110\}$ and $\{112\}$ planes at a strain of 0.4.

Lastly, Figure 12 shows the intragranular behavior of a grain C initially oriented in the $[11\bar{9}8]$ direction. The grain C was selected since it was closely aligned to $[1\bar{1}1]$ direction (Figure 12a). It rotates much less than the other two grains presented in Figure 10 and 11. Furthermore, as shown in Figure 12b and 12c, there is no significant intragranular misorientation. Dislocation densities in the grain C grow very similarly to those in a single crystal loaded in the $[1\bar{1}1]$

direction, attributed to the small rotation during deformation. As shown in Figure 12d, the dislocation densities in the grain C grow remarkably in the slip systems of $A\bar{8}$, $B1\bar{2}$ and $C1\bar{0}$ that exhibit the highest Schmid factors in a single crystal loaded in the $[1\bar{1}1]$ direction.

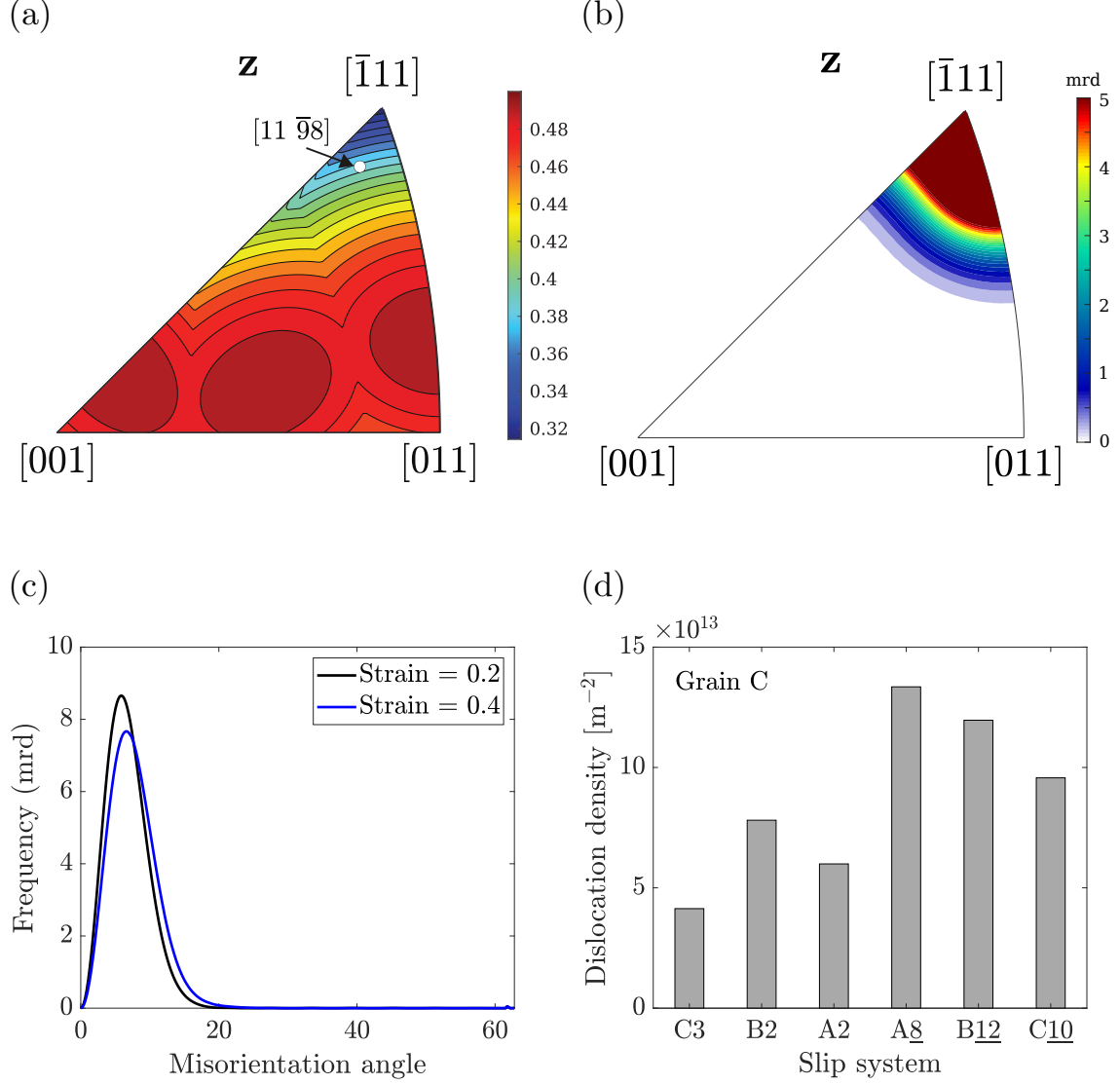


Figure. 12. Numerically predicted rotation and dislocation density in a grain C in the $[11\ \bar{9}8]$ direction within the Voronoi-tessellated polycrystal domain. (a) Location of the $[11\ \bar{9}8]$ direction on contour of the maximum Schmid factor, (b) countour of crystallographic orientations within the grain C at a strain of 0.4, (c) distribution of misorientation angle within the grain (strains of 0.2 and 0.4), (d) dislocation densities in slip systems on both $\{110\}$ and $\{112\}$ planes at a strain of 0.4.

4 Discussion and concluding remarks

Plastic deformation in bcc tantalum has been deemed a complex process which involves various length-scales. The inelastic behaviors in bcc tantalum are strongly rate- and temperature-dependent, involving complex physics in the motion of dominant screw dislocations. In past decades, continuum mechanics-based crystal plasticity theories have been proposed to address the salient features of the rate- and temperature-dependent deformation in this important refractory metallic material. Furthermore, the continuum crystal plasticity theories have enabled modeling of the large inelastic behavior of tantalum single crystals or polycrystals. In this work, we have extended the crystal plasticity model to elucidate the deformations of both single- and polycrystal tantalum materials at a wide range of strain rates and temperatures. Furthermore, using a suite of finite deformation constitutive modeling, experiments and numerical simulations, we have addressed the main features of deformation mechanisms, dislocation evolution and the hardening behavior in bcc tantalum.

At the single crystal level, we extended the finite deformation single crystal viscoplasticity model to account for the evolution and interaction of dislocation densities throughout the slip systems on both $\{110\}$ and $\{112\}$ planes. Our single crystal model takes into account the dislocation interaction strengths critically associated with the hardening behavior as well as the microstructural evolution in bcc single crystals, informed by the recent dislocation dynamics simulation results for tantalum. The single crystal model with material parameters simply calibrated with experimental data on single crystal tantalum has been shown to accurately capture the major features in the stress-strain responses at low to high strain rates and at room temperature and higher in the major crystallographic orientations of $[001]$, $[01\bar{1}]$, $[111]$ and $[\bar{1}49]$. Furthermore, using the single crystal model, we addressed the effects of collinear interactions on slip activity and instability in single crystals loaded in high symmetry orientations. The strong collinear interactions were found to give rise to bifurcation in the slip activity throughout the slip systems. The instability under high symmetry loading directions was also found to diminish with a slight misorientation. Though our single crystal model successfully captures the key features of the large inelastic behavior of single crystal tantalum at 0.001 s^{-1} to 5300 s^{-1} and at room temperature and higher, it needs to be further developed to account for low temperature behavior accompanied by the non-Schmid effects, especially on the $\{110\} \langle 111 \rangle$ slip systems. To this ends, the interaction properties throughout the slip systems must be further identified by

more improved dislocation dynamics simulations, especially below room temperature. Furthermore, our analysis for the effects of collinear interaction and misorientation on instability in the slip activity should be of critical importance in further developing the model able to capture the single crystal behavior at low temperature, in which slip on the $\{110\}$ planes are more likely to be activated.

Our single crystal model has been further underpinned by the successful representation of polycrystal behaviors in both experiments and numerical simulations. We conducted mechanical testing of polycrystal tantalum specimens together with *ex situ* neutron diffraction measurements for crystallographic textures and dislocation density at increasing strains. Numerical simulation results showed predictive capabilities of our modeling framework for the macroscopic stress-strain behavior and the corresponding crystallographic texturing at low to high strain rates and at room temperature and higher. Our polycrystal model was also shown to be capable of reproducing the Taylor’s relation in which the flow stress is linearly proportional to the square root of the dislocation density experimentally evidenced in *ex situ* neutron diffraction measurements on dislocation density growth in the polycrystal specimen at increasing strains. Furthermore, we have investigated spatial variations of rotation and dislocation density throughout the more realistic polycrystal network upon using numerical simulations on a Voronoi-tessellation-based polycrystal network. The numerically predicted local variations of the inelastic features provided critical insight into the underlying physical pictures for microstructural evolution within the individual crystals undergoing severe plastic deformation which recently have received great attention for polycrystal materials (Pokharel et al. 2014; Millett et al. 2020; Charpagne et al. 2021).

Our structurally unified modeling framework has been shown not only to reproduce the experimental data but also provide physical insight into the deformation mechanisms and microstructural evolutions in single crystal and polycrystal tantalum under plastic deformation at a broad range of strains, strain rates and temperatures. Though our model captures many important aspects of plastic deformation in bcc tantalum, much needs to be done for further refinement of the theory for bcc materials. In particular, the model as proposed is structural only and therefore does not yet account for the proper partition of energy into evolution of dislocation structure or thermal energy. This is particularly important for the ability of predicting the evolution of dislocation density and structure and properly accounting for the evolution of temperature within a thermally sensitive theory. Furthermore, there is much we do not yet

know about the mechanics and energetics of bcc dislocation behavior and interaction within the potential kink-pair mechanism of dislocation motion, particularly for the rate limiting screw dislocations and the role which edge dislocations play (Butler et al. 2018; Wang et al. 2021). Indeed, the bcc crystal plasticity theory needs to be further extended to account for the influence of grain boundaries and thereby grain size effect that critically influence the characteristics of dislocation motion in and out of grains of a polycrystal, consequently culminating in substantial change in the macroscopic inelastic features. In addition, short- or long-range spatial interactions between dislocations and grain boundaries or between different grains throughout the polycrystal network should be taken into account for accurately modeling extreme events such as damage nucleation and growth. Towards this end, the more realistic, grain boundary conforming polycrystal models must be established using the electronic backscatter diffraction and *state-of-the-art* measurement techniques for the actual microstructures for bcc materials (Foster et al. 2021).

Acknowledgement

This work was funded by National Research Foundation (NRF) of Korea (Grant No. 2020R1-C1C101324812 and 2021R1A4A103278311) and National Science Foundation (NSF) CMMI (Grant No. 2115399). This work has also benefitted from the use of the Los Alamos Neutron Science Center (LANSCE) at Los Alamos National Laboratory. Los Alamos National Laboratory is operated by Triad National Security, LLC, for the National Nuclear Security Administration of the U.S. Department of Energy under contract number 89233218NCA000001.

Appendix

A Time integration procedure for single crystal model

The implicit time integration procedure we have used in this work is summarized, as follows. Let $\tau = t + \Delta t$. Using the given,

1. $\mathbf{F}(t), \mathbf{F}(\tau),$
2. $\mathbf{F}^p(t), s^\alpha(t), \mathbf{T}(t)$

our task is to update $\{\mathbf{F}^p(\tau), s^\alpha(\tau), \rho^\alpha(\tau)$ and $\mathbf{T}(\tau)\}$.

Components of the fourth order elasticity tensor in the global basis are calculated by,

$$\mathcal{C}_{ijkl} = Q_{ip}Q_{jq}Q_{kr}Q_{lr}\mathcal{C}_{pqrs}^c, \quad (\text{A.1})$$

where \mathcal{C}_{pqrs}^c is the component of the fourth order elasticity tensor in the crystal basis and \mathbf{Q} is the orthogonal tensor which rotates the crystal basis to the global basis (e.g. Anand 2004). Trial quantities are then calculated by,

$$\mathbf{F}_{\text{tr}}^e = \mathbf{F}(\tau)\mathbf{F}^{p-1}(t), \quad (\text{A.2})$$

$$\mathbf{C}_{\text{tr}}^e = \mathbf{F}_{\text{tr}}^{eT}\mathbf{F}_{\text{tr}}^e, \quad (\text{A.3})$$

$$\mathbf{E}_{\text{tr}}^e = \frac{1}{2}(\mathbf{C}_{\text{tr}}^e - \mathbf{1}), \quad (\text{A.4})$$

$$\mathbf{T}_{\text{tr}}^e = \mathbf{C}[\mathbf{E}_{\text{tr}}^e - \mathbf{A}(\theta - \theta_0)], \quad (\text{A.5})$$

$$\mathbf{B}^\alpha = \text{symm}[\mathbf{C}_{\text{tr}}^e \mathbb{S}_0^\alpha], \quad (\text{A.6})$$

$$\mathbf{C}^\alpha = \mathbf{C} \left[\frac{1}{2} \mathbf{B}^\alpha \right]. \quad (\text{A.7})$$

The following coupled implicit equations for $\mathbf{T}^e(\tau)$, $s^\alpha(\tau)$ and $\rho^\alpha(\tau)$,

$$\mathbf{T}^e(\tau) = \mathbf{T}_{\text{tr}}^e - \sum_{\alpha=1}^N \Delta\gamma_p^\alpha(\mathbf{T}^e(\tau), s^\alpha(\tau)) \mathbf{C}^\alpha, \quad (\text{A.8})$$

$$s^\alpha(\tau) = s^\alpha(t) + \Delta s^\alpha(\Delta\gamma_p^\beta(\mathbf{T}^e(\tau), s^\beta(\tau)), \rho^\beta(\tau)), \quad (\text{A.9})$$

$$\rho^\alpha(\tau) = \rho^\alpha(t) + \Delta\rho^\alpha(\Delta\gamma_p^\alpha(\mathbf{T}^e(\tau), s^\alpha(\tau)), \rho^\beta(\tau)), \quad (\text{A.10})$$

with,

$$\Delta\gamma_p^\alpha = \Delta t \gamma_0 \exp\left(-\frac{\Delta G}{k_B\theta} \left\langle 1 - \left(\frac{|\tau^\alpha| - s^\alpha(\tau)}{\tilde{s}_l}\right)^p \right\rangle^q\right); \quad \text{where } \tau^\alpha = \mathbf{T}^e(\tau) : \mathbb{S}_0^\alpha, \quad (\text{A.11})$$

$$\begin{aligned} \Delta s^\alpha &= \Delta t \dot{s}^\alpha(\tau) \\ &= \frac{1}{2}\mu \frac{\sum_\beta a^{\alpha\beta}}{\sqrt{\sum_\beta a^{\alpha\beta}\rho^\beta(\tau)}} \left(\sqrt{\sum_\gamma d^{\beta\gamma}\rho^\gamma(\tau)} - 2y_c^\beta \rho^\beta(\tau) \right) |\Delta\gamma_p^\beta(\mathbf{T}^e(\tau), s^\beta(\tau))|, \end{aligned} \quad (\text{A.12})$$

$$\Delta\rho^\alpha = \Delta t \dot{\rho}^\alpha(\tau) = \frac{1}{b} \left(\sqrt{\sum_{\beta} d^{\alpha\beta} \rho^\beta(\tau) - 2y_c^\alpha \rho^\alpha(\tau)} \right) |\Delta\gamma_p^\alpha(\mathbf{T}^e(\tau), s^\alpha(\tau))|, \quad (\text{A.13})$$

where,

$$y_c^\alpha = y_{c0} \left(1 - \frac{k_B \theta}{A_{rec}} \ln \left| \frac{\Delta\gamma_p^\alpha}{\Delta t \dot{\gamma}_0} \right| \right), \quad (\text{A.14})$$

are solved using the following two-step iteration procedure.

First, the elastic 2nd Piola stress is updated, keeping $s^\alpha(\tau)$ and $\rho^\alpha(\tau)$ fixed, by,

$$\mathbf{T}_{n+1}^e(\tau) = \mathbf{T}_n^e(\tau) - \mathcal{J}_n^{-1}[\mathbf{G}_n], \quad (\text{A.15})$$

$$\mathbf{G}_n \equiv \mathbf{T}_n^e(\tau) - \mathbf{T}_{tr}^e + \sum_{\alpha=1}^N \Delta\gamma_p^\alpha(\mathbf{T}_n^e(\tau), s_k^\alpha(\tau)) \mathbf{C}^\alpha, \quad (\text{A.16})$$

$$\mathcal{J}_n \equiv \mathcal{I} + \sum_{\alpha=1}^N \mathbf{C}^\alpha \otimes \frac{\partial}{\partial \mathbf{T}_n^e(\tau)} \Delta\gamma_p^\alpha(\mathbf{T}_n^e(\tau), s_k^\alpha(\tau)), \quad (\text{A.17})$$

where \mathcal{I} is the fourth-order identity tensor. The elastic 2nd Piola stress is accepted if,

$$\left| [\mathcal{J}_n^{-1}[\mathbf{G}_n]]_{ij} \right| < \Delta T_{tol}^e, \quad (\text{A.18})$$

where ΔT_{tol}^e is the tolerance for stress. The Newton correction in Equation (A.15) is accepted if,

$$\max_{\alpha} |\Delta\gamma_p^\alpha(\mathbf{T}_{n+1}^e(\tau), s_k^\alpha(\tau))| < \Delta\gamma_{p, tol}, \quad (\text{A.19})$$

where $\Delta\gamma_{p, tol}$ is the upper bound for the incremental shear strain rate. Here, we have used $\Delta\gamma_{p, tol} = 0.5$. However, if the constraint in Equation (A.19) is not satisfied, the elastic stress (\mathbf{T}_{n+1}^e) is further corrected by,

$$[T_{n+1}^e(\tau)]_{ij} = [T_n^e(\tau)]_{ij} + \eta \Delta T_{ij}^e, \quad (\text{A.20})$$

where $\Delta \mathbf{T}^e = -\mathcal{J}_n^{-1}[\mathbf{G}_n]$ and η is the correction factor. Here, we have used $\eta = 0.25$. This correction is repeated until the corrected elastic stress satisfies the constraint.

Using the converged $\mathbf{T}^e(\tau)$, the slip resistance ($s^\alpha(\tau)$) and the dislocation density ($\rho^\alpha(\tau)$)

are simply updated with no iterations by,

$$\begin{aligned} s_{k+1}^\alpha(\tau) &= s^\alpha(t) + \Delta s^\alpha\left(\Delta\gamma_p^\beta(\mathbf{T}_{n+1}^e(\tau), s_k^\beta(\tau)), \rho_k^\beta\right) \\ &= s^\alpha(t) + \frac{1}{2}\mu \frac{\sum_\beta a^{\alpha\beta}}{\sqrt{\sum_\beta a^{\alpha\beta}\rho_k^\beta}} \left(\sqrt{\sum_\gamma d^{\beta\gamma}\rho_k^\gamma} - 2y_c^\beta \rho_k^\beta \right) |\Delta\gamma_p^\beta(\mathbf{T}_{n+1}^e(\tau), s_k^\beta(\tau))|, \end{aligned} \quad (\text{A.21})$$

and

$$\begin{aligned} \rho_{k+1}^\alpha(\tau) &= \rho^\alpha(t) + \Delta\rho^\alpha\left(\Delta\gamma_p^\alpha(\mathbf{T}_{n+1}^e(\tau), s_k^\alpha(\tau)), \rho_k^\beta\right) \\ &= \rho^\alpha(t) + \frac{1}{b} \left(\sqrt{\sum_\beta d^{\alpha\beta}\rho_k^\beta} - 2y_c^\alpha \rho_k^\alpha \right) |\Delta\gamma_p^\alpha(\mathbf{T}_{n+1}^e(\tau), s_k^\beta(\tau))|. \end{aligned} \quad (\text{A.22})$$

The slip resistance is accepted if,

$$\max_\alpha |s_{k+1}^\alpha - s_k^\alpha| < s_{\text{tol}}^\alpha. \quad (\text{A.23})$$

If not accepted, we go back to the first level of the iteration procedure in Equation (A.15) upon using the updated values, s_{k+1}^α and ρ_{k+1}^α .

Once $\mathbf{T}^e(\tau)$, $s^\alpha(\tau)$, $\rho^\alpha(\tau)$ in the two-step iteration procedure are accepted, the kinematic variables are then updated. The Cauchy stress and the temperature at the end of the increment are then updated by Equations (14) and (22), respectively.

B Computation of material Jacobian

The implicit finite element procedure employed in this work uses a Newton-type iteration which requires a fourth order tangent also known as Jacobian at the end of the increment defined by,

$$\mathbf{W}(\tau) \equiv \frac{\partial \mathbf{T}(\tau)}{\partial \mathbf{E}_t(\tau)}, \quad (\text{B.1})$$

where $\mathbf{T}(\tau)$ is the Cauchy stress and $\mathbf{E}_t(\tau)$ is the symmetric relative strain tensor⁴. The Cauchy stress is calculated by,

$$\mathbf{T}(\tau) = \frac{1}{\det \mathbf{F}^e(\tau)} [\mathbf{F}^e(\tau) \mathbf{T}^e(\tau) \mathbf{F}^{eT}(\tau)]. \quad (\text{B.2})$$

⁴The relative deformation gradient is defined as $\mathbf{F}_t(\tau) = \mathbf{F}(\tau) \mathbf{F}^{-1}(t)$. Similar to the deformation gradient, the relative deformation gradient tensor also allows for the polar decomposition, $\mathbf{F}_t(\tau) = \mathbf{R}_t(\tau) \mathbf{U}_t(\tau)$ where \mathbf{R}_t is relative rotation tensor and \mathbf{U}_t is relative stretch tensor. The relative strain tensor is then defined as $\mathbf{E}_t(\tau) = \ln \mathbf{U}_t(\tau)$. (Balasubramanian 1998)

From Equation (B.2) we have,

$$d\mathbf{T} = \frac{1}{\det \mathbf{F}^e} [d\mathbf{F}^e \mathbf{T}^e \mathbf{F}^{eT} + \mathbf{F}^e d\mathbf{T}^e \mathbf{F}^{eT} + \mathbf{F}^e \mathbf{T}^e d\mathbf{F}^{eT} - (\mathbf{F}^e \mathbf{T}^e \mathbf{F}^{eT}) \text{tr}(d\mathbf{F}^e \mathbf{F}^{e-1})]. \quad (\text{B.3})$$

Hence, the tangent tensor is expressed by,

$$\mathcal{W}_{ijkl} = \frac{1}{\det \mathbf{F}^e} [\mathcal{S}_{imkl} T_{mn}^e F_{nj}^{eT} + F_{im}^e \mathcal{Q}_{mnkl} F_{nj}^{eT} + F_{im}^e T_{mn}^e \mathcal{S}_{jnkl} - F_{im}^e T_{mn}^e F_{nj}^{eT} \mathcal{S}_{pqkl} F_{qp}^{e-1}], \quad (\text{B.4})$$

with

$$\mathcal{S} \equiv \frac{\partial \mathbf{F}^e}{\partial \mathbf{E}_t} \quad \text{and} \quad \mathcal{Q} \equiv \frac{\partial \mathbf{T}^e}{\partial \mathbf{E}_t}. \quad (\text{B.5})$$

Since the relative stretch is small in this work,

$$\mathbf{E}_t = \ln \mathbf{U}_t \approx \mathbf{U}_t - \mathbf{1}, \quad (\text{B.6})$$

Where \mathbf{U}_t is the relative stretch tensor. Therefore, $d\mathbf{E}_t \approx d\mathbf{U}_t$ and the fourth order tensor \mathcal{S} and \mathcal{Q} is expressed by,

$$\mathcal{S} = \frac{\partial \mathbf{F}^e}{\partial \mathbf{U}_t} \quad \text{and} \quad \mathcal{Q} = \frac{\partial \mathbf{T}^e}{\partial \mathbf{U}_t}. \quad (\text{B.7})$$

(1) Calculation of \mathcal{S}

The elastic deformation gradient at τ can be obtained by,

$$\mathbf{F}^e(\tau) = \mathbf{F}(\tau) \mathbf{F}^{p-1}(\tau) = \mathbf{R}_t \mathbf{U}_t \mathbf{F}^e(t) \left\{ \mathbf{1} - \sum_{\alpha=1}^N \Delta \gamma_p^\alpha \mathbb{S}_0^\alpha \right\}. \quad (\text{B.8})$$

Then,

$$\begin{aligned} \mathcal{S}_{ijkl} &= \frac{\partial F_{ij}^e}{\partial U_{(t)kl}} = \frac{\partial}{\partial U_{(t)kl}} \left[R_{(t)im} U_{(t)mn} F_{np}^e(t) \left\{ \delta_{pj} - \sum_{\alpha=1}^N \Delta \gamma_p^\alpha \mathbb{S}_{0pj}^\alpha \right\} \right] \\ &= R_{(t)ik} F_{lj}^e(t) - R_{(t)ik} F_{lp}^e(t) \sum_{\alpha=1}^N \Delta \gamma_p^\alpha \mathbb{S}_{0pj}^\alpha - R_{(t)im} U_{(t)mn} F_{np}^e(t) \sum_{\alpha=1}^N \mathcal{R}_{kl}^\alpha \mathbb{S}_{0pj}^\alpha, \end{aligned} \quad (\text{B.9})$$

with $\mathcal{R}^\alpha = \frac{\partial \Delta \gamma_p^\alpha}{\partial \mathbf{U}_t}$, and subscript (t) denotes relative quantities.

(2) Calculation of \mathcal{Q}

From Equation (A.8)

$$\mathcal{Q}_{ijkl} = \frac{\partial T_{ij}^e}{\partial U_{(t)kl}} = \mathcal{D}_{ijkl} - \sum_{\alpha=1}^N \mathcal{R}_{kl}^{\alpha} C_{ij}^{\alpha} - \sum_{\alpha=1}^N \Delta \gamma_p^{\alpha} \mathcal{J}_{ijkl}^{\alpha}, \quad (\text{B.10})$$

where $\mathcal{D} = \frac{\partial \mathbf{T}_{\text{tr}}^e}{\partial \mathbf{U}_t}$ and $\mathcal{J}^{\alpha} = \frac{\partial \mathbf{C}^{\alpha}}{\partial \mathbf{U}_t}$. \mathcal{D} is expressed by,

$$\mathcal{D}_{ijkl} = \frac{\partial T_{(tr)ij}^e}{\partial U_{(t)kl}} = \frac{1}{2} \mathcal{C}_{ijmn} \mathcal{L}_{mnkl}. \quad (\text{B.11})$$

And \mathcal{L} is calculated by,

$$\begin{aligned} \mathcal{L}_{ijkl} &= \frac{\partial C_{(tr)ij}^e}{\partial U_{(t)kl}} = \frac{\partial}{\partial U_{(t)kl}} \left[F_{mi}^{p-1}(t) F_{nm}(\tau) F_{np}(\tau) F_{pj}^{p-1}(t) \right] \\ &= \frac{\partial}{\partial U_{(t)kl}} \left[F_{mi}^e(t) U_{(t)mn}(\tau) U_{(t)np}(\tau) F_{pj}^e(t) \right] \\ &= F_{mi}^e(t) \delta_{mk} \delta_{nl} U_{(t)np} F_{pj}^e(t) + F_{mi}^e(t) U_{(t)mn} \delta_{nk} \delta_{pl} F_{pj}^e(t) \\ &= F_{ki}^e(t) U_{(t)lp} F_{pj}^e(t) + F_{mi}^e(t) U_{(t)mk} F_{lj}^e(t). \end{aligned} \quad (\text{B.12})$$

Furthermore, from Equations (A.6) and (A.7), \mathcal{J}^{α} is calculated by,

$$\begin{aligned} \mathcal{J}_{ijkl}^{\alpha} &= \frac{\partial C_{ij}^{\alpha}}{\partial U_{(t)kl}} = \frac{\partial}{\partial U_{(t)kl}} \left[\frac{1}{2} \mathcal{C}_{ijmn} (C_{(tr)mp} \mathbb{S}_{0pn}^{\alpha} + \mathbb{S}_{0pm}^{\alpha} C_{(tr)pn}) \right] \\ &= \frac{1}{2} \left[\mathcal{C}_{ijmn} \mathcal{L}_{mpkl} \mathbb{S}_{0pn}^{\alpha} + \mathcal{C}_{ijmn} \mathbb{S}_{0pm}^{\alpha} \mathcal{L}_{pnkl} \right]. \end{aligned} \quad (\text{B.13})$$

Moreover, \mathcal{R}^{α} is calculated by,

$$\mathcal{R}_{ij}^{\alpha} = \frac{\partial \Delta \gamma_p^{\alpha}(\mathbf{T}^e)}{\partial U_{(t)ij}} = \frac{\partial \Delta \gamma_p^{\alpha}(\mathbf{T}^e)}{\partial T_{kl}^e} \frac{\partial T_{kl}^e}{\partial U_{(t)ij}} = \mathcal{B}_{kl}^{\alpha} \mathcal{Q}_{klij}, \quad (\text{B.14})$$

with

$$\mathcal{B}_{ij}^{\alpha} = \frac{\partial \Delta \gamma_p^{\alpha}}{\partial T_{ij}^e} = \frac{\partial \Delta \gamma_p^{\alpha}}{\partial \tau^{\alpha}} \frac{\partial \tau^{\alpha}}{\partial T_{ij}^e} = \frac{\partial \Delta \gamma_p^{\alpha}}{\partial \tau^{\alpha}} \frac{1}{2} (\mathbb{S}_{0ij}^{\alpha} + \mathbb{S}_{0ji}^{\alpha}). \quad (\text{B.15})$$

\mathcal{Q} is therefore expressed by,

$$\mathcal{Q} = \mathcal{D} - \sum_{\alpha=1}^N (\mathbf{C}^{\alpha} \otimes \mathcal{B}^{\alpha}) \mathcal{Q} - \sum_{\alpha=1}^N \Delta \gamma_p^{\alpha} \mathcal{J}^{\alpha}. \quad (\text{B.16})$$

Then, rearranging Equation (B.16), we have,

$$\mathcal{Q} = \left[\mathcal{I} + \sum_{\alpha=1}^N (\mathbf{C}^\alpha \otimes \mathbf{B}^\alpha) \right]^{-1} \left[\mathcal{D} - \sum_{\alpha=1}^N \Delta \gamma_p^\alpha \mathcal{J}^\alpha \right], \quad (\text{B.17})$$

$$\mathcal{K} \equiv \mathcal{I} + \sum_{\alpha=1}^N (\mathbf{C}^\alpha \otimes \mathbf{B}^\alpha), \quad (\text{B.18})$$

$$\mathcal{M} \equiv \mathcal{D} - \sum_{\alpha=1}^N \Delta \gamma_p^\alpha \mathcal{J}^\alpha. \quad (\text{B.19})$$

The computation of the tangent is summarized as follows,

1. $\mathbf{U}_t = \mathbf{R}_t^{-1} \mathbf{F}(\tau) \mathbf{F}^{-1}(t),$
2. $\mathcal{C}_{ijkl} = Q_{ip} Q_{jq} Q_{kr} Q_{lr} \mathcal{C}_{pqrs}^c,$
3. $\mathcal{L}_{ijkl} = F_{ki}^e(t) U_{(t)lp} F_{pj}^e(t) + F_{mi}^e(t) U_{(t)mk} F_{lj}^e(t),$
4. $\mathcal{D}_{ijkl} = \frac{1}{2} \mathcal{C}_{ijmn} \mathcal{L}_{mnkl},$
5. $\mathcal{J}_{ijkl}^\alpha = \frac{1}{2} \left[\mathcal{C}_{ijmn} \mathcal{L}_{mpkl} \mathbb{S}_{0pn}^\alpha + \mathcal{C}_{ijmn} \mathbb{S}_{0pm}^\alpha \mathcal{L}_{pnkl} \right],$
6. $\mathcal{B}_{ij}^\alpha = \frac{\partial \Delta \gamma_p^\alpha}{\partial \tau^\alpha} \frac{1}{2} (\mathbb{S}_{0ij}^\alpha + \mathbb{S}_{0ji}^\alpha),$
7. $\mathcal{K}_{ijkl} = \delta_{ik} \delta_{jl} + \sum_{\alpha=1}^N C_{ij}^\alpha \mathcal{B}_{kl}^\alpha, \text{ (Calculated in reduced form } \mathcal{K}_{IJ})$
8. $\mathcal{M}_{ijkl} = \mathcal{D}_{ijkl} - \sum_{\alpha=1}^N \Delta \gamma_p^\alpha \mathcal{J}_{ijkl}^\alpha. \text{ (Calculated in reduced form } \mathcal{M}_{IJ})$
9. $\mathcal{Q}_{ijkl} = \mathcal{K}_{ijmn}^{-1} \mathcal{M}_{mnkl} \text{ (Calculated in reduced form } \mathcal{Q}_{IJ})$
10. $\mathcal{R}_{ij}^\alpha = \mathcal{B}_{kl}^\alpha \mathcal{Q}_{kl ij},$
11. $\mathcal{S}_{ijkl} = R_{(t)ik} F_{lj}^e - R_{(t)ik} F_{lp}^e \sum_{\alpha=1}^N \Delta \gamma_p^\alpha \mathbb{S}_{0pj}^\alpha - R_{(t)im} U_{(t)mn} F_{np}^e \sum_{\alpha=1}^N \mathcal{R}_{kl}^\alpha \mathbb{S}_{0pj}^\alpha,$
12. $\mathcal{W}_{ijkl} = \frac{1}{\det \mathbf{F}^e} [\mathcal{S}_{imkl} T_{mn}^e F_{nj}^{eT} + F_{im}^e \mathcal{Q}_{mnkl} F_{nj}^{eT} + F_{im}^e T_{mn}^e \mathcal{S}_{jnkl} - F_{im}^e T_{mn}^e F_{nj}^{eT} \mathcal{S}_{pqkl} F_{qp}^{e-1}]$

References

- Anand, Lallit (2004). “Single-crystal elasto-viscoplasticity: application to texture evolution in polycrystalline metals at large strains”. *Computer Methods in Applied Mechanics and Engineering* 193.48–51, pp. 5359–5383.
- Asaro, R J and A Needleman (1985). “Overview no. 42 Texture development and strain hardening in rate dependent polycrystals”. *Acta Metallurgica* 33.6, pp. 923–953.
- Asaro, Robert J (1983). “Micromechanics of Crystals and Polycrystals”. Ed. by John W Hutchinson and Theodore Y Wu. Vol. 23. Advances in Applied Mechanics. Elsevier, pp. 1–115.
- Bachmann, F., R. Hielscher, and H. Schaeben (2010). “Texture analysis with MTEX- Free and open source software toolbox”. *Solid State Phenomena* 160, pp. 63–68.
- Balasubramanian, Srihari (1998). “Polycrystalline plasticity : application to deformation processing of lightweight metals”. PhD thesis. Massachusetts Institute of Technology.
- Bever, Michael Berliner, David Lewis Holt, and Alan Lee Titchener (1973). “The stored energy of cold work”. *Progress in materials science* 17, pp. 5–177.
- Beyerlein, I. J. and C. N. Tomé (2008). “A dislocation-based constitutive law for pure Zr including temperature effects”. *International Journal of Plasticity* 24.5, pp. 867–895.
- Bronkhorst, C. A., G. T. Gray, F. L. Addessio, V. Livescu, N. K. Bourne, S. A. McDonald, and P. J. Withers (2016). “Response and representation of ductile damage under varying shock loading conditions in tantalum”. *Journal of Applied Physics* 119.8, p. 085103.
- Bronkhorst, C. A., J. R. Mayeur, V. Livescu, R. Pokharel, D. W. Brown, and G. T. Gray (2019). “Structural representation of additively manufactured 316L austenitic stainless steel”. *International Journal of Plasticity* 118, pp. 70–86.
- Bronkhorst, C. A., H. Cho, P. W. Marcy, S. A. Vander Wiel, S. Gupta, D. Versino, V. Anghel, and G. T. Gray (2021). “Local micro-mechanical stress conditions leading to pore nucleation during dynamic loading”. *International Journal of Plasticity* 137, p. 102903.
- Bronkhorst, C.A., E.K. Cerreta, Q. Xue, P.J. Maudlin, T.A. Mason, and G.T. Gray (2006). “An experimental and numerical study of the localization behavior of tantalum and stainless steel”. *International Journal of Plasticity* 22.7, pp. 1304–1335.
- Bronkhorst, Curt A, S. R. Kalidindi, and Lallit Anand (1992). “Polycrystalline plasticity and the evolution of crystallographic texture in FCC metals”. *Philosophical Transactions of the Royal Society of London. Series A: Physical and Engineering Sciences* 341.1662, pp. 443–477.
- Brown, D. W., M. A. Okuniewski, T. A. Sisneros, B. Clausen, G. A. Moore, and L. Balogh (2016). “Neutron diffraction measurement of residual stresses, dislocation density and texture in Zr-bonded U-10Mo “mini” fuel foils and plates”. *Journal of Nuclear Materials* 482, pp. 63–74.
- Butler, Brady G, James D Paramore, Jonathan P Ligda, Chai Ren, Z Zak Fang, Scott C Middlemas, and Kevin J Hemker (2018). “Mechanisms of deformation and ductility in tungsten—A review”. *International Journal of Refractory Metals and Hard Materials* 75, pp. 248–261.
- Byron, J. F. (1968). “Plastic deformation of tantalum single crystals. II. The orientation dependence of yield”. *Journal of The Less-Common Metals* 14.2, pp. 201–210.

- Cereceda, David, Martin Diehl, Franz Roters, Dierk Raabe, J. Manuel Perlado, and Jaime Marian (2016). “Unraveling the temperature dependence of the yield strength in single-crystal tungsten using atomistically-informed crystal plasticity calculations”. *International Journal of Plasticity* 78, pp. 242–265.
- Charpagne, M. A., J. M. Hestroffer, A. T. Polonsky, M. P. Echlin, D. Texier, V. Valle, I. J. Beyerlein, T. M. Pollock, and J. C. Stinville (2021). “Slip localization in Inconel 718: A three-dimensional and statistical perspective”. *Acta Materialia* 215, p. 117037.
- Chen, Shuh Rong and George T. Gray (1996). “Constitutive behavior of tantalum and tantalum-tungsten alloys”. *Metallurgical and Materials Transactions A: Physical Metallurgy and Materials Science* 27, pp. 2994–3006.
- Cho, Hansohl, Curt A Bronkhorst, Hashem M Mourad, Jason R Mayeur, and D J Luscher (2018). “Anomalous plasticity of body-centered-cubic crystals with non-Schmid effect”. *International Journal of Solids and Structures* 139-140, pp. 138–149.
- Cuitiño, A. M. and M. Ortiz (1993). “Computational modelling of single crystals”. *Modelling and Simulation in Materials Science and Engineering* 1.3, pp. 225–263.
- Dai, Hong (1997). “Geometrically-necessary dislocation density in continuum plasticity theory, FEM implementation and applications”. PhD thesis. Massachusetts Institute of Technology.
- Dequiedt, J. L. and C. Denoual (2021). “Localization of plastic deformation in stretching sheets with a crystal plasticity approach: Competition between weakest link and instable mode controlled process”. *International Journal of Solids and Structures* 210-211, pp. 183–202.
- Dequiedt, J. L., C. Denoual, and R. Madec (2015). “Heterogeneous deformation in ductile FCC single crystals in biaxial stretching: the influence of slip system interactions”. *Journal of the Mechanics and Physics of Solids* 83, pp. 301–318.
- Devincre, B., L. Kubin, and T. Hoc (2006). “Physical analyses of crystal plasticity by DD simulations”. *Scripta Materialia* 54.5, pp. 741–746.
- Devincre, Benoit, Thierry Hoc, and Ladislav P. Kubin (2005). “Collinear interactions of dislocations and slip systems”. *Materials Science and Engineering: A* 400-401, pp. 182–185.
- Dezerald, L., L. Proville, Lisa Ventelon, F. Willaime, and D. Rodney (2015). “First-principles prediction of kink-pair activation enthalpy on screw dislocations in bcc transition metals: V, Nb, Ta, Mo, W, and Fe”. *Physical Review B - Condensed Matter and Materials Physics* 91.9, pp. 1–7.
- Dezerald, Lucile, David Rodney, Emmanuel Clouet, Lisa Ventelon, and François Willaime (2016). “Plastic anisotropy and dislocation trajectory in BCC metals”. *Nature Communications* 7.1, p. 11695.
- Dieter, George Ellwood and David J Bacon (1976). *Mechanical metallurgy*. Vol. 3. McGraw-hill New York.
- Dorogoy, A and D Rittel (2017). “Dynamic large strain characterization of tantalum using shear-compression and shear-tension testing”. *Mechanics of Materials* 112, pp. 143–153.
- Duesbery, M. S., V. Vitek, Bowen, and David Keith (1973). “The effect of shear stress on the screw dislocation core structure in body-centred cubic lattices”. *Proceedings of the Royal Society of London. A. Mathematical and Physical Sciences* 332.1588, pp. 85–111.
- Farren, William Scott and Geoffrey Ingram Taylor (1925). “The heat developed during plastic extension of metals”. *Proceedings of the Royal Society of London. Series A* 107.743, pp. 422–451.

- Foster, Robert C, Scott Vander Wiel, Veronica Anghel, and Curt Bronkhorst (2021). “Towards random generation of microstructures of spatially varying materials from orthogonal sections”. *Computational Materials Science* 192, p. 110313.
- Gröger, R., A. G. Bailey, and V. Vitek (2008a). “Multiscale modeling of plastic deformation of molybdenum and tungsten: I. Atomistic studies of the core structure and glide of $1/2\langle 111 \rangle$ screw dislocations at 0 K”. *Acta Materialia* 56.19, pp. 5401–5411.
- Gröger, R., V. Racherla, J. L. Bassani, and V. Vitek (2008b). “Multiscale modeling of plastic deformation of molybdenum and tungsten: II. Yield criterion for single crystals based on atomistic studies of glide of $1/2\langle 111 \rangle$ screw dislocations”. *Acta Materialia* 56.19, pp. 5412–5425.
- Gurtin, Morton E. (2000). “On the plasticity of single crystals: Free energy, microforces, plastic-strain gradients”. *Journal of the Mechanics and Physics of Solids* 48.5, pp. 989–1036.
- Hill, R. and J. R. Rice (1972). “Constitutive analysis of elastic-plastic crystals at arbitrary strain”. *Journal of the Mechanics and Physics of Solids* 20.6, pp. 401–413.
- Hoge, K. G. and A. K. Mukherjee (1977). “The temperature and strain rate dependence of the flow stress of tantalum”. *Journal of Materials Science* 12.8, pp. 1666–1672.
- Ismail-Beigi, Sohra and T. A. Arias (2000). “Ab initio study of screw dislocations in mo and Ta: A new picture of plasticity in bcc transition metals”. *Physical Review Letters* 84.7, pp. 1499–1502.
- Kalidindi, S. R., C. A. Bronkhorst, and L. Anand (1992). “Crystallographic texture evolution in bulk deformation processing of FCC metals”. *Journal of the Mechanics and Physics of Solids* 40.3, pp. 537–569.
- Knezevic, Marko, Irene J. Beyerlein, Manuel L. Lovato, Carlos N. Tomé, Andrew W. Richards, and Rodney J. McCabe (2014). “A strain-rate and temperature dependent constitutive model for BCC metals incorporating non-Schmid effects: Application to tantalum-tungsten alloys”. *International Journal of Plasticity* 62, pp. 72–92.
- Kocks, U. F. (1976). “Laws for Work-Hardening and Low-Temperature Creep”. *Journal of Engineering Materials and Technology* 98.1, pp. 76–85.
- Kocks, U Fred, Carlos Norberto Tomé, and H-R Wenk (1998). *Texture and anisotropy: preferred orientations in polycrystals and their effect on materials properties*. Cambridge university press.
- Kothari, M. and L. Anand (1998). “Elasto-viscoplastic constitutive equations for polycrystalline metals: Application to tantalum”. *Journal of the Mechanics and Physics of Solids* 46.1, pp. 51–67.
- Kraus, R. G., F. Coppari, D. E. Fratanduono, R. F. Smith, A. Lazicki, C. Wehrenberg, J. H. Eggert, J. R. Rygg, and G. W. Collins (2021). “Melting of Tantalum at Multimegabar Pressures on the Nanosecond Timescale”. *Physical Review Letters* 126.25, p. 255701.
- Lieou, Charles KC and Curt A Bronkhorst (2020). “Thermodynamic theory of crystal plasticity: formulation and application to polycrystal fcc copper”. *Journal of the Mechanics and Physics of Solids* 138, p. 103905.
- (2021). “Thermomechanical conversion in metals: dislocation plasticity model evaluation of the Taylor-Quinney coefficient”. *Acta Materialia* 202, pp. 170–180.
- Lim, H., L.M. Hale, J.A. Zimmerman, C.C. Battaile, and C.R. Weinberger (2015a). “A multi-scale model of dislocation plasticity in α -Fe: Incorporating temperature, strain rate and non-Schmid effects”. *International Journal of Plasticity* 73, pp. 100–118.

- Lim, Hojun, Corbett C. Battaile, Jay D. Carroll, Brad L. Boyce, and Christopher R. Weinberger (2015b). “A physically based model of temperature and strain rate dependent yield in BCC metals: Implementation into crystal plasticity”. *Journal of the Mechanics and Physics of Solids* 74, pp. 80–96.
- Lim, Hojun, Jay D. Carroll, Joseph R. Michael, Corbett C. Battaile, Shuh Rong Chen, and J. Matthew D. Lane (2020). “Investigating active slip planes in tantalum under compressive load: Crystal plasticity and slip trace analyses of single crystals”. *Acta Materialia* 185, pp. 1–12.
- Losko, Adrian S., Sven C. Vogel, H. Matthias Reiche, and Heinz Nakotte (2014). “A six-axis robotic sample changer for high-throughput neutron powder diffraction and texture measurements”. *Journal of Applied Crystallography* 47.6, pp. 2109–2112.
- Ma, A. and F. Roters (2004). “A constitutive model for fcc single crystals based on dislocation densities and its application to uniaxial compression of aluminium single crystals”. *Acta Materialia* 52.12, pp. 3603–3612.
- Ma, A., F. Roters, and D. Raabe (2007). “A dislocation density based constitutive law for BCC materials in crystal plasticity FEM”. *Computational Materials Science* 39.1, pp. 91–95.
- Madec, R., B. Devincere, L. Kubin, T. Hoc, and D. Rodney (2003). “The role of collinear interaction in dislocation-induced hardening”. *Science* 301.5641, pp. 1879–1882.
- Madec, Ronan and Ladislav P. Kubin (2017). “Dislocation strengthening in FCC metals and in BCC metals at high temperatures”. *Acta Materialia* 126, pp. 166–173.
- Matsuno, Hironobu, Atsuro Yokoyama, Fumio Watari, Motohiro Uo, and Takao Kawasaki (2001). “Biocompatibility and osteogenesis of refractory metal implants, titanium, hafnium, niobium, tantalum and rhenium”. *Biomaterials* 22.11, pp. 1253–1262.
- Matthies, S., J. Pehl, H. R. Wenk, L. Lutterotti, and S. C. Vogel (2005). “Quantitative texture analysis with the HIPPO neutron TOF diffractometer”. *Journal of Applied Crystallography* 38.3, pp. 462–475.
- Mayeur, J. R., I. J. Beyerlein, C. A. Bronkhorst, H. M. Mourad, and B. L. Hansen (2013). “A crystal plasticity study of heterophase interface character stability of Cu/Nb bicrystals”. *International Journal of Plasticity* 48, pp. 72–91.
- Miehe, Christian, Jörg Schröder, and Jan Schotte (1999). “Computational homogenization analysis in finite plasticity simulation of texture development in polycrystalline materials”. *Computer Methods in Applied Mechanics and Engineering* 171.3-4, pp. 387–418.
- Millett, J. C.F., P. Avraam, G. Whiteman, D. J. Chapman, and S. Case (2020). “The role of orientation on the shock response of single crystal tantalum”. *Journal of Applied Physics* 128.3, p. 035104.
- Monnet, G. and B. Devincere (2006). “Solute friction and forest interaction”. *Philosophical Magazine* 86.11, pp. 1555–1565.
- Narayanan, Sankar, David L. McDowell, and Ting Zhu (2014). “Crystal plasticity model for BCC iron atomistically informed by kinetics of correlated kinkpair nucleation on screw dislocation”. *Journal of the Mechanics and Physics of Solids* 65, pp. 54–68.
- Nemat-Nasser, Sia, Tomoo Okinaka, and Luqun Ni (1998). “A physically-based constitutive model for BCC crystals with application to polycrystalline tantalum”. *Journal of the Mechanics and Physics of Solids* 46.6, pp. 1009–1038.

- Nguyen, Thao, Saryu J. Fensin, and Darby J. Luscher (2021). “Dynamic crystal plasticity modeling of single crystal tantalum and validation using Taylor cylinder impact tests”. *International Journal of Plasticity* 139, p. 102940.
- Pappu, S., C. Kennedy, L. E. Murr, and M. A. Meyers (1996). “Deformation twins in a shock-loaded Ta-2.5w/oW precursor plate and a recovered, Ta-2.5w/oW explosively formed penetrator”. *Scripta Materialia* 35.8, pp. 959–965.
- Patra, Anirban, Ting Zhu, and David L. McDowell (2014). “Constitutive equations for modeling non-Schmid effects in single crystal bcc-Fe at low and ambient temperatures”. *International Journal of Plasticity* 59, pp. 1–14.
- Pokharel, Reeju, Jonathan Lind, Anand K. Kanjarla, Ricardo A. Lebensohn, Shiu Fai Li, Peter Kenesei, Robert M. Suter, and Anthony D. Rollett (2014). “Polycrystal plasticity: Comparison between grain - Scale observations of deformation and simulations”. *Annual Review of Condensed Matter Physics* 5.1, pp. 317–346.
- Quey, R., P. R. Dawson, and F. Barbe (2011). “Large-scale 3D random polycrystals for the finite element method: Generation, meshing and remeshing”. *Computer Methods in Applied Mechanics and Engineering* 200.17-20, pp. 1729–1745.
- Queyreau, Sylvain, Ghiath Monnet, and Benoît Devincre (2009). “Slip systems interactions in α -iron determined by dislocation dynamics simulations”. *International Journal of Plasticity* 25.2, pp. 361–377.
- Ribárik, G., J. Gubicza, and T. Ungár (2004). “Correlation between strength and microstructure of ball-milled Al-Mg alloys determined by X-ray diffraction”. *Materials Science and Engineering A* 387-389, pp. 343–347.
- Rietveld, H. M. (1969). “A profile refinement method for nuclear and magnetic structures”. *Journal of Applied Crystallography* 2.2, pp. 65–71.
- Rittel, D, M L Silva, B Poon, and G Ravichandran (2009). “Thermomechanical behavior of single crystalline tantalum in the static and dynamic regime”. *Mechanics of Materials* 41.12, pp. 1323–1329.
- Rittel, D, AA Kidane, M Alkhader, A Venkert, P Landau, and G Ravichandran (2012). “On the dynamically stored energy of cold work in pure single crystal and polycrystalline copper”. *Acta Materialia* 60.9, pp. 3719–3728.
- Rittel, D, LH Zhang, and S Osovski (2017). “The dependence of the Taylor–Quinney coefficient on the dynamic loading mode”. *Journal of the Mechanics and Physics of Solids* 107, pp. 96–114.
- Sherwood, P. J., F. Guiu, H. C. Kim, and P. L. Pratt (1967). “Plastic Anisotropy of Tantalum, Niobium, and Molybdenum”. *Canadian Journal of Physics* 45.2, pp. 1075–1089.
- Stainier, L., A.M. Cuitiño, and M. Ortiz (2002). “A micromechanical model of hardening, rate sensitivity and thermal softening in BCC single crystals”. *Journal of the Mechanics and Physics of Solids* 50.7, pp. 1511–1545.
- Takajo, Shigehiro and Sven C. Vogel (2018). “Determination of pole figure coverage for texture measurements with neutron time-of-flight diffractometers”. *Journal of Applied Crystallography* 51.3, pp. 895–900.
- Taylor, G. (1928). “Section A. -Mathematical and physical sciences. - The deformation of crystals of β -brass”. *Proceedings of the Royal Society of London. Series A* 118.779, pp. 1–24.
- Taylor, G. and C. F. Elam (1926). “The distortion of iron crystals”. *Proceedings of the Royal Society of London. Series A* 112.761, pp. 337–361.

- Taylor, Geoffrey Ingram (1938). “Plastic strain in metals”. *J. Inst. Metals* 62, pp. 307–324.
- Taylor, Geoffrey Ingram and H Quinney (1934). “The latent energy remaining in a metal after cold working”. *Proceedings of the Royal Society of London. Series A* 143.849, pp. 307–326.
- Titchener, Alan Lee and Michael Berliner Bever (1958). “The stored energy of cold work”. *Progress in metal physics* 7, pp. 247–338.
- Vogel, Sven C., Christian Hartig, Luca Lutterotti, Robert B. Von Dreele, Hans-Rudolf Wenk, and Darrick J. Williams (2004). “Texture measurements using the new neutron diffractometer HIPPO and their analysis using the Rietveld method”. *Powder Diffraction* 19.1, pp. 65–68.
- Wang, Xiaowang, Shuozhi Xu, Wu-Rong Jian, Xiang-Guo Li, Yanqing Su, and Irene J Beyerlein (2021). “Generalized stacking fault energies and Peierls stresses in refractory body-centered cubic metals from machine learning-based interatomic potentials”. *Computational Materials Science* 192, p. 110364.
- Wenk, H. R., L. Lutterotti, and S. Vogel (2003). “Texture analysis with the new HIPPO TOF diffractometer”. *Nuclear Instruments and Methods in Physics Research, Section A: Accelerators, Spectrometers, Detectors and Associated Equipment* 515.3, pp. 575–588.
- Wenk, H.-R., L. Lutterotti, and S. C. Vogel (2010). “Rietveld texture analysis from TOF neutron diffraction data”. *Powder Diffraction* 25.3, pp. 283–296.
- Whiteman, G, S Case, J C F Millett, M J Cox, P Avraam, J P Dear, A Sancho, and P A Hooper (2019). “Uniaxial compression of single crystal and polycrystalline tantalum”. *Materials Science and Engineering A* 759, pp. 70–77.
- Yalcinkaya, T, W A M Brekelmans, and M G D Geers (2008). “BCC single crystal plasticity modeling and its experimental identification”. *Modelling and Simulation in Materials Science and Engineering* 16.8, p. 085007.
- Yang, L. H., P. Söderlind, and J. A. Moriarty (2001). “Accurate atomistic simulation of $(a/2) \langle 111 \rangle$ screw dislocations and other defects in bcc tantalum”. *Philosophical Magazine A* 81.5, pp. 1355–1385.